Journal of Theoretical Biology 511 (2021) 110541

Contents lists available at ScienceDirect

Journal of Theoretical Biology

journal homepage: www.elsevier.com/locate/yjtbi

A Monte Carlo method to estimate cell population heterogeneity from cell snapshot data

Ben Lambert [a,b,*], David J. Gavaghan [c], Simon J. Tavener [d]

[a] Department of Zoology, University of Oxford, Oxford, Oxfordshire, UK
[b] MRC Centre for Global Infectious Disease Analysis, School of Public Health, Imperial College London, London W2 1PG, UK
[c] Department of Computer Science, University of Oxford, Oxford, UK
[d] Department of Mathematics, Colorado State University, Fort Collins, Colorado, USA

ARTICLE INFO

Article history:
Received 24 October 2019
Revised 16 July 2020
Accepted 10 November 2020
Available online 30 November 2020

Keywords:
Cellular heterogeneity
Bayesian inference
Single cell data
Inverse problems

ABSTRACT

Variation is characteristic of all living systems. Laboratory techniques such as flow cytometry can probe individual cells, and, after decades of experimentation, it is clear that even members of genetically identical cell populations can exhibit differences. To understand whether variation is biologically meaningful, it is essential to discern its source. Mathematical models of biological systems are tools that can be used to investigate causes of cell-to-cell variation. From mathematical analysis and simulation of these models, biological hypotheses can be posed and investigated, then parameter inference can determine which of these is compatible with experimental data. Data from laboratory experiments often consist of "snapshots" representing distributions of cellular properties at different points in time, rather than individual cell trajectories. These data are not straightforward to fit using hierarchical Bayesian methods, which require the number of cell population clusters to be chosen *a priori*. Nor are they amenable to standard nonlinear mixed effect methods, since a single observation per cell is typically too few to estimate parameter variability. Here, we introduce a computational sampling method named "Contour Monte Carlo" (CMC) for estimating mathematical model parameters from snapshot distributions, which is straightforward to implement and does not require that cells be assigned to predefined categories. The CMC algorithm fits to snapshot probability distributions rather than raw data, which means its computational burden does not, like existing approaches, increase with the number of cells observed. Our method is appropriate for underdetermined systems, where there are fewer distinct types of observations than parameters to be determined, and where observed variation is mostly due to variability in cellular processes rather than experimental measurement error. This may be the case for many systems due to continued improvements in resolution of laboratory techniques. In this paper, we apply our method to quantify cellular variation for three biological systems of interest and provide Julia code enabling others to use this method.

1. Introduction

Variation, as opposed to homogeneity, is the rule rather than exception in biology. Indeed, without variation, biology as a discipline would not exist, since as evolutionary biologist JBS Haldane wrote, variation is the "raw material" of evolution. The Red Queen Hypothesis asserts organisms must continually evolve in order to survive when pitted against other – also evolving – organisms (Ridley, 1994). A corollary of this hypothesis is that multicellular organisms should evolve cellular phenotypic heterogeneity to allow faster adaptation to changing environments, which may explain the observed variation in a range of biological systems (Fraser and Kaern, 2009). Whilst cell population variation can confer evolutionary advantages, it can be costly in other circumstances. In biotechnological processes, heterogeneity in cellular function can reduce yields of biochemical products (Delvigne et al., 2014). In human biology, variation across cells can enable pathologies to develop; it can also frustrate treatment of illness because key subpopulations are missed by medical interventions that target "average" cell properties. For example, cellular heterogeneity helps some cancerous tumours to persist (Gatenby et al., 2007) and can make tumours more likely to evolve resistance to chemotherapies (Altrock et al., 2015). To discern whether observed

* Corresponding author at: Department of Zoology, University of Oxford, Oxford, Oxfordshire, UK.
E-mail address: ben.c.lambert@gmail.com (B. Lambert).

https://doi.org/10.1016/j.jtbi.2020.110541
0022-5193/

variation is benign or requires remedy, methods of analysis are needed that can quantify and help to understand its source.

Mathematical models are essential tools for understanding cellular systems, whose emergent properties are the result of a nexus of interactions between actors. Perhaps the simplest flavour of mathematical model used in biological systems is an ordinary differential equation (ODE) that aggregates individual actors into compartments according to structure or function and seeks to model the mean behaviour of each compartment. Data from population-averaged experimental assays can determine whether such models faithfully reproduce system behaviours and can be used to understand the structure of complex metabolic, signalling and transcriptional networks. The worth of such "population average" ODE models depends on whether averages mask substantial differences in individual behaviour (Altschuler and Wu, 2010). In some cases, differences in cellular protein abundances due to biochemical "noise" are not biologically meaningful (Elowitz et al., 2002) and the system is well described by average cell behaviour. In others, there are functional consequences. For example, a laboratory study demonstrated that subpopulations of clonally-derived hematopoietic progenitor cells with low expression of a stem cell marker diverged into a separate blood lineage from those with high expression (Chang et al., 2008).

Many modelling frameworks are available to describe cell population heterogeneity with each posing different challenges for parameter inference. A recent review is presented in Waldherr (2018). These approaches include modelling biochemical processes stochastically, where properties of ensembles of cells are represented by probability distributions that evolve according to chemical master equations. See Erban et al. (2007) for a tutorial on stochastic simulation of reaction diffusion processes. Alternatively, population balance equations (PBEs) are typically partial integro-differential equations that determine the dynamics of the "number density" of differing cell types. In PBEs, cell properties are represented as points in $\mathbb{R}^n$, with each dimension corresponding to a different attribute. These attributes include parameters controlling cell life – for example, their rate of death and division, which vary according to a cell's location in this "attribute" space. These functional differences control the rate at which cells progress through life, which is represented by a "flow" of cells from certain areas of attribute space to others – like chemicals diffusing down a concentration gradient. With PBEs, observed variation at a point in time is due to the initial spread of cells across attribute space coupled with the differing dynamics of cells in different areas of this space. See Ramkrishna and Singh (2014) for an introduction to PBEs.

Here, we suppose heterogeneity in quantities of interest across cells is generated by idiosyncratic variation in the rates of cellular processes. The modelling approach we follow is similar to that of Dixit et al. (2018) and is based on an ODE framework. In our model, each cell evolves according to an ODE, with its progression directed by parameters whose value varies between cells. To our knowledge, this flavour of model is unnamed, so, for sake of reference, we call them "heterogenous ODE" models (HODEs). In HODEs, the aim of inference is to estimate distributions of parameter values across cells consistent with observations. A benefit of using HODEs is that these models are computationally straightforward to simulate and, arguably, simpler to parameterise than PBEs. By using HODEs, we assume that most observed variation comes from differences in biological processes across cells, not inherent stochasticity in biochemical reactions within cells as is assumed when employing stochastic simulations algorithms.

Inference for HODEs is problematic due, partly, to the experimental hurdles involved with generating data of sufficient standard. Unlike models which represent a population by a single scalar ODE, since HODEs are individual-based, they ideally require individual cell data for estimation. A widely-used method for generating such data is flow cytometry, where a large number of cells are streamed individually through a laser beam, and, for example, the concentrations of fluorescently-labelled proteins are measured (Telford et al., 2012). Other experimental techniques, including Western blotting and cytometric fluorescence microscopy, can also generate single cell measurements (Hughes et al., 2014; Hasenauer et al., 2011). These experimental methods are all, however, destructive, meaning individual cells are sacrificed during measurement, and observations at each time point hence represent "*snapshots*" of the underlying population (Hasenauer et al., 2011). These snapshots can be described by histograms (Dixit et al., 2018) or density functions (Waldherr, 2018) fit to measurements of quantities of interest.

Since HODEs assume the state of each cell evolves continuously over time, experimental data tracing individual cell trajectories through time constitutes a richer data resource. Fluorescent Recovery After Photo-bleaching (FRAP) is one such method, which follows the time-dependent response of cells after an initial bleaching (Karlsson et al., 2015). Methods exists, broadly under the banner of "nonlinear mixed effects models", which use cell trajectories – individual time series of cellular quantities – to estimate both cellular variation and qualities of measurement noise. See, for example, Karlsson et al. (2015), Zechner et al. (2014), and Dharmarajan et al. (2019). The demands of obtaining such data are, however, higher and typically involve either tracking individual cells through imaging methods (Hilsenbeck et al., 2016), or trapping cells in a spatial position where they can be monitored over time (Fritzsch et al., 2012). These techniques impose severe restrictions on experimental practices meaning they cannot be used in many circumstances, including for online monitoring of biotechnological processes or analysis of *in vivo* studies. "Snapshot" data continues to play an important role for determining cell level variability in many applications, and, in this paper, we restrict analysis to only such data.

By fitting HODEs to snapshot data, cellular variability can be estimated, and a number of approaches have been proposed for doing so. In HODEs, parameter values vary across cells according to a to-be-determined probability distribution, and the solution to the inverse problem requires solving the cell-specific ODE system many times for each individual. The count of cells in experiments typically exceeds $\sim 10^4$ (Hasenauer et al., 2011), so approaches where the computational burden scales with this count are usually infeasible. There are two current approaches for dealing with this burden, and both involve dimensionality reduction. In other words, both approaches require preprocessing raw data before analysis, so result in a degree of information loss. The first involves using population average data – mean values of measurements at different points in time – yet, explicitly model how this mean represents a mixture across different subpopulations. Chan et al. (2016) follow this approach to analyse population substructure in immune cells, which allows them to employ standard Bayesian approaches to fitting. The alternative approach is to fit probability densities to raw snapshot data and use these densities, rather than raw data, for estimation (Hasenauer et al., 2011; Hasenauer et al., 2014; Loos et al., 2018; Dixit et al., 2018). We follow this approach here as it is likely that more information about the underlying data is retained than in the "population average" one.

We now briefly describe the existing approaches for using HODE models to estimate cell population heterogeneity. Hasenauer et al. (2011) present a Bayesian approach to inference for HODEs, which models the input parameter space using an ansatz of a mixture of densities of chosen types. The authors then use their method to reproduce population substructure on synthetic data generated from a model of tumour necrosis factor stim-

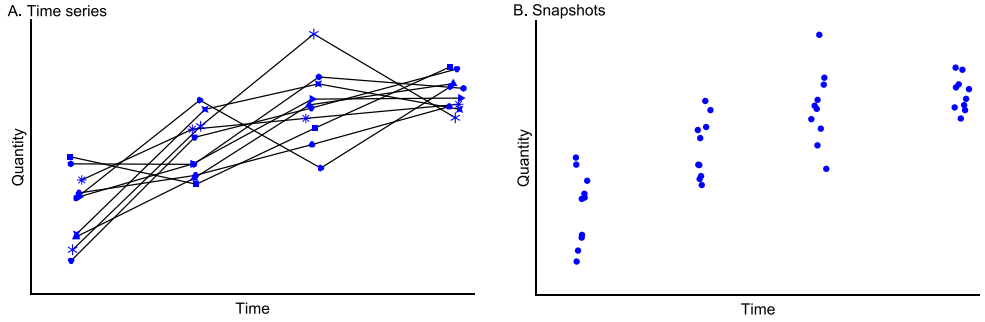

Fig. 1. Data typical of single cell experiments. (A) Time series data. (B) Snapshot data. In A, note cell identities are retained at each measurement time (indicated by individual plot markers), whereas in the snapshot data in B, either this information is lost, or more often, cells are destroyed by the measurement process, and each observation corresponds to a distinct cell.

ulus. Hasenauer et al. (2014) use mixture models to model subpopulation structure in snapshot data with multiple-start local optimisation employed to maximise the non-convex likelihood, which they then apply to synthetic and real data from signalling pathway models. Loos et al. (2018) also use mixture models to represent subpopulation structure and use maximum likelihood to estimate both within- and between-subpopulation variability, which permits fitting to multivariate output distributions with complex correlation structures. Dixit et al. (2018) assign observations into discrete bins, then choose likelihood distributions according to the maximum entropy criterion, which they then use to estimate cell variability within a Bayesian framework.

Our framework is Bayesian although it is distinct from the approach used to fit many dynamic models, since we assume output variation arises from parameter heterogeneity across cells, with no contribution from measurement noise. The approach is, hence, most suitable when measurement error is minimal. Additionally, our approach is suitable only for underdetermined models – which we define as the case where there are fewer output quantities of interest than parameters. Since the generation of snapshots is expensive, it is often the case that fewer observables are recorded than parameters. Hence, we believe that this restriction does not present particular issue to the generalisability of our approach. Our method is a two-step Monte Carlo approach, which, for reasons described in §2, we call "Contour Monte Carlo" (CMC). Unlike many existing methods, CMC is straightforward to implement and does not require extensive computation time. In CMC, prior probability distributions are used in place of ansatz densities. It also does not require the number of cell clusters be chosen beforehand, rather, subpopulations emerge as modes in the posterior parameter distributions. Like Loos et al. (2018), CMC can fit multivariate snapshot data and unlike Dixit et al. (2018), does not use discrete bins to model continuous data. As more experimental techniques elucidating single cell behaviour are developed, interest in models describing measurement snapshots should follow. We argue that due to its simplicity and generality, CMC can be used to perform inference on the proliferation of rich single cell data and, thus, is a useful addition to the modeller's toolkit.

Outline of the paper: In §2, we describe our probabilistic model of the inverse problem and detail the CMC algorithm for generating samples from the posterior parameter distribution. In §3, we use CMC to estimate cell population heterogeneity in three systems of biological interest.

2. Method

In this section, we first develop a probabilistic framework that describes our inverse problem before introducing the CMC algorithm in pseudocode (Algorithm 1). We also detail the workflow we have found helpful in using CMC to analyse cell snapshot data (Fig. 4), and suggest practical remedies to issues commonly encountered while using this approach. A glossary of variable names used in this paper is included as Table 1.

Table 1
Glossary of variable names used in this paper.

Variable	Definition	Dimension
$\boldsymbol{x}(t)$	ODE solution	$\mathbb{R}^k$
$\boldsymbol{\theta}$	ODE parameters	$\mathbb{R}^p$
$\boldsymbol{f}(\boldsymbol{x}(t);\boldsymbol{\theta})$	ODE RHS	$\mathbb{R}^k$
$\boldsymbol{x}^{\{i\}}(t)$	ODE solution for cell i	$\mathbb{R}^k$
$q_j = q_j(\boldsymbol{x}(t_j);\boldsymbol{\theta}) = q_j(\boldsymbol{\theta})$	quantity of interest (QOI) j	$\mathbb{R}^1$
$\boldsymbol{q}^\top = (q_1,\ldots,q_m)$	m distinct QOIs	$\mathbb{R}^m$
$q_j^{\{i\}} = q_j(\boldsymbol{x}^{\{i\}}(t_j))$	QOI j for cell i	$\mathbb{R}^1$
$\boldsymbol{y}_j^\top = \left(q_j^{\{1\}},\ldots q_j^{\{n_j\}}\right)$	QOI j for cells $1,\ldots,n_j$	$\mathbb{R}^{n_j}$
$\boldsymbol{Y} = (\boldsymbol{y}_1,\ldots,\boldsymbol{y}_m)$	"snapshot" of all QOIs	$(\mathbb{R}^{n_1}\times\mathbb{R}^{n_2}\times\ldots\times\mathbb{R}^{n_m})$
Φ	parameters of output target distribution, $p(\boldsymbol{q}\|\Phi)$	$\mathbb{R}^m$
Ξ	parameters of prior parameter distribution, $p(\boldsymbol{\theta}\|\Xi)$	$\mathbb{R}^p$
Ψ	parameters of prior output distribution, $p(\boldsymbol{q}\|\Psi)$	$\mathbb{R}^p$
$\hat{a}$	estimates of any quantity a	–
$\Omega(\boldsymbol{z})$	region of parameter space mapping to $\boldsymbol{q}=\boldsymbol{z}$	$\mathbb{R}^{\leqslant p}$
$\measuredangle(\boldsymbol{z})$	volume of $\Omega(\boldsymbol{z})$	$\mathbb{R}^+$
V	volume of (bounded) parameter space	$\mathbb{R}^+$
$a^{[n]}$	nth sample of any quantity a	-

Experimental methods such as flow cytometry measure single cell characteristics at a given time. Cells are typically destroyed by the measurement process, so the data consists of cross-sections or "snapshots" of sampled individuals from the population rather than providing time series for each individual cell. The contrast between these two very different scenarios is highlighted in Fig. 1. For snapshot data, the cells at time t_k are not the same as those at time t_{k-1}, and, even if they are, there is no way of associating a particular cell at time t_k with the same cell at time t_{k-1}. In other words, there is no sense of a "trajectory" of a specific cell, or of multiple observations assigned to a single cell.

We model the processes of an individual cell using a system of ordinary differential equations (ODEs), where each element of the system typically corresponds to the concentration of a particular species. Our initial value problem is,

$$\frac{d\boldsymbol{x}}{dt} = \boldsymbol{f}(\boldsymbol{x}(t);\boldsymbol{\theta}), \quad \boldsymbol{f} : \mathbb{R}^k \times \mathbb{R}^p \mapsto \mathbb{R}^k, \quad \boldsymbol{x}(0) = \boldsymbol{x_0}. \tag{1}$$

Note that in most circumstances, the initial state of the system, $\boldsymbol{x}(0)$, is unknown, and it can be convenient to include these as elements of $\boldsymbol{\theta}$ to be estimated.

2.1. Snapshot data

We assume the variation in snapshots arises due to heterogeneity in the underlying parameters, $\boldsymbol{\theta}$, across cells. Therefore, the evolution of the underlying state of cell i is described by an idiosyncratic ODE,

$$\begin{aligned} &\frac{d\boldsymbol{x}^{\{i\}}}{dt} = \boldsymbol{f}\left(\boldsymbol{x}^{\{i\}}(t);\boldsymbol{\theta}^{\{i\}}\right), \quad \boldsymbol{f} : \mathbb{R}^k \times \mathbb{R}^p \mapsto \mathbb{R}^k, \\ &\boldsymbol{x}^{\{i\}}(0) = \boldsymbol{x_0}. \end{aligned} \tag{2}$$

where superscript $^{\{i\}}$ indicates the ith cell. The collection of such idiosyncratic ODEs across all cells is then referred to as the "HODE model".

The traditional (non-hierarchical) state-space approach to modelling dynamic systems supposes that measurement error introduces stochastic variation in the output (Fig. 2A). Our approach, by contrast, assumes any variation in outputs is solely due to variation in parameter values between cells (Fig. 2B). Whether the assumption of "perfect" measurements is reasonable depends on experimental details of the system under investigation, but we argue our method nevertheless provides a useful approximation in cases where the signal to noise ratio is high. Once again we emphasize that we are considering distributions of quantities of interest with no sense of specific individual trajectories, making a mixed effects modelling approach problematic.

In an experiment, quantities of interest (QOIs) are measured. Examples of QOIs include concentrations of compounds at different points in time, peak voltages across cell membranes during an action potential, or measurements of cell volume. Here, we suppose $m \geqslant 1$ QOIs are measured,

$$\boldsymbol{q}^\top = (q_1, q_2, \ldots, q_m) \in \mathbb{R}^m, \tag{3}$$

with n_j observations of each quantity, q_j. Distinct QOIs, q_j, may correspond to different functionals of the solution at the same time or the same functional at different times. The observed data for QOI q_j at the corresponding time t_j consists of the n_j cellular measurements,

$$\boldsymbol{y}(t_j)^\top = \left(q_j(x^{\{1\}}(t_j)), q_j(x^{\{2\}}(t_j)), \ldots, q_j\left(x^{\{n_j\}}(t_j)\right)\right) \in \mathbb{R}^{n_j}. \tag{4}$$

The raw snapshot data $\boldsymbol{Y}$ is the collection of all measured QOIs,

$$\boldsymbol{Y} = (\boldsymbol{y}(t_1), \boldsymbol{y}(t_2), \ldots, \boldsymbol{y}(t_m)) \in \mathbb{R}^{n_1} \times \mathbb{R}^{n_2} \times \ldots \times \mathbb{R}^{n_m}. \tag{5}$$

The goal of inference is to characterise the probability distribution $p(\boldsymbol{\theta}|\boldsymbol{Y})$ representing heterogeneity in cellular processes. The numbers of cells sampled in typical experimental setups is large, and, following previous work, we represent snapshot data $\boldsymbol{Y}$ using probability distributions (Hasenauer et al., 2011; Hasenauer et al., 2014; Loos et al., 2018; Dixit et al., 2018). In the first step of our workflow (Fig. 4(i)), these distributions are approximated by a kernel density model with support over the space of the QOI vector, $\boldsymbol{q} \in \mathbb{R}^m$. We suppose these kernel density estimates approximate a true distribution over the observed data, $p(\boldsymbol{q}|\Phi)$ and

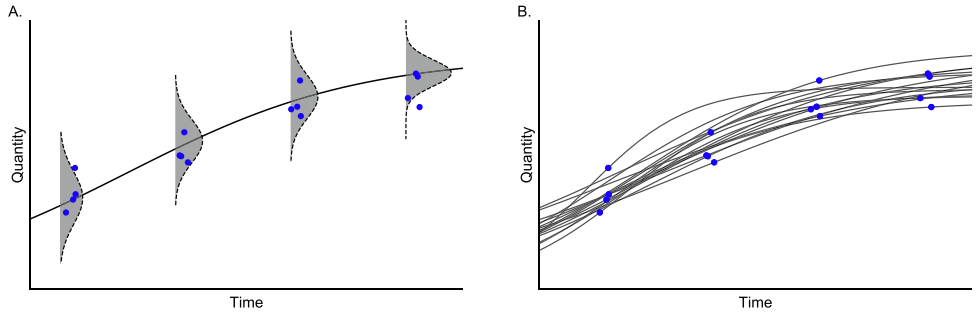

Fig. 2. Models of variation in observed outputs. (A) State-space model. (B) Parameter heterogeneity model. (A) For non-hierarchical state-space models, there is a single "true" latent state, and observations result from an imperfect measurement process (grey histograms). (B) For models with parameter heterogeneity, the uncertainty is generated by differences in cellular processes (black lines) between cells. Note that, in both cases, individual cells are measured only once in their lifetime.

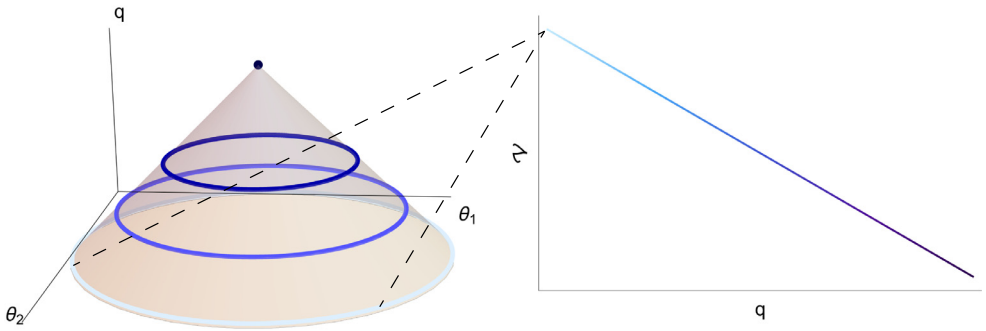

Fig. 3. Left: An example output function $q(\theta_1, \theta_2)$ along with iso-output contours indicated (coloured lines). Right: The "volume" of output contours as a function of output value. Note that here, since parameter space is two dimensional, the "volume" of each output value corresponds to a length of an iso-output contour.

denote the estimated density as $p\left(\boldsymbol{q}|\hat{\Phi}\right)$. After this initial fitting, this distribution – which we term the "target distribution" – becomes the object we seek to replicate in our inference problem. We assume there are enough observational data that the estimated probability distributions are approximate sufficient statistics of the posterior distribution, meaning $p\left(\boldsymbol{\theta}|\hat{\Phi}\right) \approx p(\boldsymbol{\theta}|\boldsymbol{Y})$.

The aim of our inverse problem, hence, becomes to derive a "posterior" parameter distribution, which, when fed through the deterministic transformation described by the model, $\boldsymbol{q}(\boldsymbol{\theta})$, recapitulates the fitted output density,

$$p\left(\boldsymbol{\theta}|\hat{\Phi}\right) \xrightarrow{\boldsymbol{q}(\boldsymbol{\theta})} p\left(\boldsymbol{q}|\hat{\Phi}\right). \tag{6}$$

In measure theoretic terms, the intrinsic measure $p\left(\boldsymbol{q}|\hat{\Phi}\right)$ implied by $p\left(\boldsymbol{\theta}|\hat{\Phi}\right)$ is known as the *push forward* of the measure with respect to the model (Butler et al., 2018).

2.2. Theoretical development of CMC

We consider the under-determined case where there are fewer QOIs than model parameters ($m < p$). This means that, provided a given QOI can be generated by the model, it can be produced from any member of a subset of parameter space. Unlike the fully-determined case, these subsets (in general) have non-zero "volume", and we term them "iso-output contour regions". Symbolically, we represent the iso-output contour region for a given quantity of interest $\tilde{\boldsymbol{q}}$ (say) by $\Omega(\tilde{\boldsymbol{q}}) = \{\boldsymbol{\theta} : \boldsymbol{q}(\boldsymbol{\theta}) = \tilde{\boldsymbol{q}}\}$.

In general, contour "volumes" $\mathscr{V}(\tilde{\boldsymbol{q}})$ depend on the chosen output value $\tilde{\boldsymbol{q}}$ (Fig. 3). Further, the interpretation of these "volumes" depends upon their dimensions. Considering cases with a single QOI: for a model with two parameters, iso-output contour regions are one-dimensional lines, whose size is a length; for a model with three parameters, the contour regions are surfaces, whose size is an area; for four-dimensional parameter spaces, the contour regions are three-dimensional, and their size is a volume; and for models with $p > 4$ parameters, the contour regions are $p-1$ dimensional manifolds, whose size is a hypervolume.

MCMC methods aim to approximate a posterior parameter distribution by sampling from it. In this case, the resultant parameter samples, when pushed through the model, should approximate samples from the desired QOI distribution. "Vanilla" MCMC methods, like Random Walk Metropolis (Lambert, 2018), work fine in more traditional Bayesian analyses but are biased for our inference problem. Such vanilla MCMC samplers choose where next to step based on the ratio of probability densities at the proposed parameter value and current position. Using a vanilla sampler for our case, unfortunately, does not work because the Markov chains are biased towards those regions of parameter space with the largest iso-output contour volumes. This bias means that the stationary parameter distribution obtained, when fed through the model, does not recapitulate the observed output distribution (Lambert et al., 2018). We stress again the difference between this problem and a traditional Bayesian analysis: here, uncertainty is due to the forward map being many-to-fewer meaning that the inverse map is indeterminant; in Bayesian inference, it comes from stochastic processes in the system itself. This difference means traditional inference methods cannot be used and motivates the method we introduce here.

Sampling algorithms, therefore, need to explicitly account for the differential volume of iso-output contours. In applied problems, however, we do not know the volumes of iso-output contours and they cannot be exactly calculated for all but the simplest models. Instead in CMC, we estimate them. The following analysis provides a brief introduction to a probabilistic formulation of under-determined inverse problems (see our companion paper Lambert et al., 2018 for a more comprehensive discussion). In doing so, this suggests a sampling based approach for estimating contour volumes, which are then exploited by our CMC algorithm.

Solving our inverse problem requires determining the posterior distribution of parameter values, $p\left(\boldsymbol{\theta}|\hat{\Phi}\right)$, which, when used as input to the forward map, results in the target distribution, $p\left(\boldsymbol{q}|\hat{\Phi}\right)$. To derive the posterior parameter distribution, we consider the joint density of parameters and QOIs, $p\left(\boldsymbol{\theta},\boldsymbol{q}|\hat{\Phi}\right)$. This can be decomposed in two ways using the law of conditional probability,

$$p\left(\boldsymbol{\theta},\boldsymbol{q}|\hat{\Phi}\right) = p\left(\boldsymbol{\theta}|\boldsymbol{q},\hat{\Phi}\right) \times p\left(\boldsymbol{q}|\hat{\Phi}\right) = p\left(\boldsymbol{q}|\boldsymbol{\theta},\hat{\Phi}\right) \times p\left(\boldsymbol{\theta}|\hat{\Phi}\right). \tag{7}$$

Rearranging Eq. (7), we obtain the posterior parameter distribution,

$$p\left(\boldsymbol{\theta}|\hat{\Phi}\right) = \frac{p\left(\boldsymbol{\theta}|\boldsymbol{q},\hat{\Phi}\right) \times p\left(\boldsymbol{q}|\hat{\Phi}\right)}{p\left(\boldsymbol{q}|\boldsymbol{\theta},\hat{\Phi}\right)}. \tag{8}$$

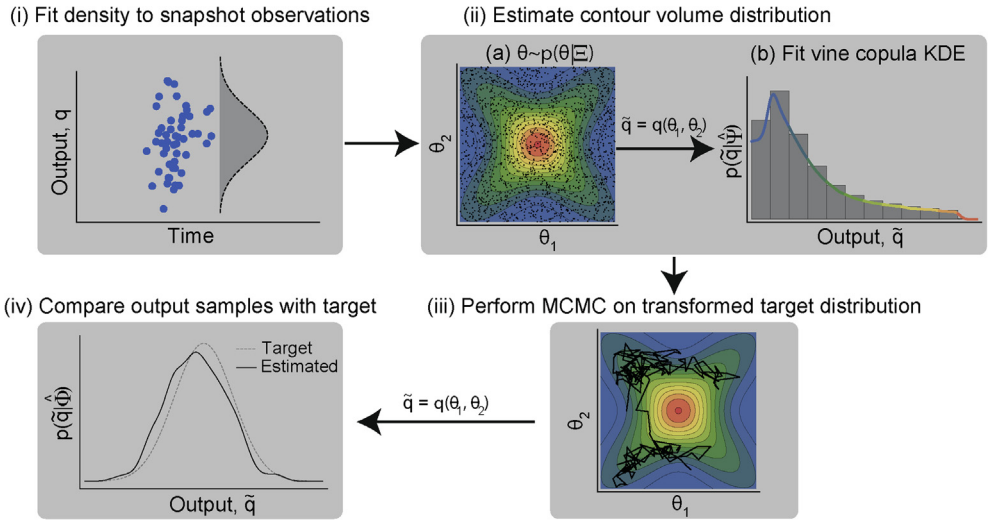

Fig. 4. Workflow for Contour Monte Carlo to estimate cell population heterogeneity. The distribution targeted in (iii) is given by Eq. (13). Here, $\tilde{q}$ is used to represent an output value resultant from applying the functional q to parameter samples (θ_1, θ_2).

Algorithm 1 Pseudocode for the Contour Monte Carlo algorithm for sampling from the posterior parameter distribution of Eq. (13).

procedure CMC($\boldsymbol{Y}, \Xi, N_1, N_2$) ▷ Sample from posterior parameter distribution
  $\hat{\Phi} = \mathit{SnapshotEstimator}(\boldsymbol{Y})$
  $\hat{\Psi} = \mathit{ContourVolumeEstimator}(\Xi, N_1)$
  $\left(\boldsymbol{\theta}^{[1]}, \ldots, \boldsymbol{\theta}^{[N_2]}\right) = \mathit{MCMC}(\hat{\Phi}, \Xi, \hat{\Psi}, N_2)$
  converged $= \mathit{CompareOutputToTarget}((\boldsymbol{\theta}^{[1]}, \ldots, \boldsymbol{\theta}^{[N_2]}), \hat{\Phi})$
  while converged $\neq 1$ ▷ Rerun contour volume estimation (if necessary modify vine copula KDE hyperparmeters) and/or MCMC, with larger sample sizes if required
    $\hat{\Psi} = \mathit{ContourVolumeEstimator}(\Xi, N_1'), \quad \mathit{where}\ N_1' \geqslant N_1$
    $\left(\boldsymbol{\theta}^{[1]}, \ldots, \boldsymbol{\theta}^{[N_2\prime]}\right) = \mathit{MCMC}(\hat{\Phi}, \Xi, \hat{\Psi}, N_2'), \quad \mathit{where}\ N_2' \geqslant N_2$
    converged $= \mathit{CompareOutputToTarget}((\boldsymbol{\theta}^{[1]}, \ldots, \boldsymbol{\theta}^{[N_2\prime]}), \hat{\Phi})$
    $N_1 \leftarrow N_1\prime,\ N_2 \leftarrow N_2\prime$
  end while
  return $\left(\boldsymbol{\theta}^{[1]}, \ldots, \boldsymbol{\theta}^{[N_2]}\right)$
end procedure
procedure SnapshotEstimator($\boldsymbol{Y}$) ▷ Fit snapshots with kernel density estimator (KDE)
  $\hat{\Phi} = \underset{\Phi}{\operatorname{argmax}} \quad p(\boldsymbol{Y}|\Phi)$
  return $\hat{\Phi}$
end procedure
procedure ContourVolumeEstimator(Ξ, N_1) ▷ Estimate volume of contours
  for i in $1 : N_1$
    $\boldsymbol{\theta}^{[i]} \sim p(\boldsymbol{\theta}|\Xi)$ ▷ Sample from prior density
    $\boldsymbol{q}^{[i]} = \boldsymbol{q}\left(\boldsymbol{\theta}^{[i]}\right)$ ▷ Calculate corresponding output value
  end for
  $\hat{\Psi} = \underset{\Psi}{\operatorname{argmax}} \quad p((\boldsymbol{q}^{[1]}, \ldots, \boldsymbol{q}^{[N_1]})|\Psi)$
    ▷ Fit vine copula KDE
  return $\hat{\Psi}$
procedure MCMC($(\hat{\Phi}, \Xi, \hat{\Psi}, N_2)$) ▷ Random Walk Metropolis algorithm targeting posterior parameter distribution
  $\boldsymbol{\theta}^{[0]} \sim \pi(.)$ ▷ Sample from arbitrary initialisation distribution
  for i in $1 : N_2$
    $\boldsymbol{\theta}^{[i]'} \sim \mathcal{N}\left(\boldsymbol{\theta}^{[i-1]}, \boldsymbol{\Sigma}\right)$ ▷ Propose new parameter values
    ▷ Calculate Metropolis acceptance ratio
    $r = p\left(\boldsymbol{\theta}^{[i]'}|\Xi\right)\ p\left(\boldsymbol{q}\left(\boldsymbol{\theta}^{[i-1]}\right)|\hat{\Psi}\right)\ p\left(\boldsymbol{q}\left(\boldsymbol{\theta}^{[i]'}\right)|\hat{\Phi}\right) / \left[p\left(\boldsymbol{\theta}^{[i-1]}|\Xi\right)\ p\left(\boldsymbol{q}\left(\boldsymbol{\theta}^{[i]'}\right)|\hat{\Psi}\right)\ p\left(\boldsymbol{q}\left(\boldsymbol{\theta}^{[i-1]}\right)|\hat{\Phi}\right)\right]$
    $u \sim U(0, 1)$ ▷ Sample from uniform distribution
    if $r > u$
      $\boldsymbol{\theta}^{[i]} = \boldsymbol{\theta}^{[i]'}$ ▷ Accept proposal
    else
      $\boldsymbol{\theta}^{[i]} = \boldsymbol{\theta}^{[i-1]}$ ▷ Reject proposal
    end if
  end for
  return $\left(\boldsymbol{\theta}^{[1]}, \ldots, \boldsymbol{\theta}^{[N_2]}\right)$
end procedure
procedure CompareOutputToTarget($(\boldsymbol{\theta}^{[1]}, \ldots, \boldsymbol{\theta}^{[N_2]}), \hat{\Phi}$) ▷ Check output distribution close to target
  for i in $1 : N_2$
    $\tilde{\boldsymbol{q}}^{[i]} = \boldsymbol{q}\left(\boldsymbol{\theta}^{[i]}\right)$ ▷ Compute QOIs for each parameter sample
  end for
  if $p(\tilde{\boldsymbol{q}}) \approx p\left(\tilde{\boldsymbol{q}}|\hat{\Phi}\right)$? ▷ Compare sampled output distribution with target
    return 1 ▷ If sufficiently close then converged
  else
    return 0
  end if
end procedure

For a deterministic map, Eq. (8) is only well defined when $\boldsymbol{q} = \boldsymbol{q}(\boldsymbol{\theta})$. (Since the mapping from parameters to outputs is deterministic, $p\left(\boldsymbol{q}|\boldsymbol{\theta}, \hat{\Phi}\right) = \delta(\boldsymbol{q}(\boldsymbol{\theta}))$, i.e., the Dirac delta function centred at $\boldsymbol{q} = \boldsymbol{q}(\boldsymbol{\theta})$.) Thus Eq. (8) becomes,

$$p\left(\boldsymbol{\theta}|\hat{\Phi}\right) = p\left(\boldsymbol{\theta}|\boldsymbol{q}(\boldsymbol{\theta}), \hat{\Phi}\right) \times p\left(\boldsymbol{q}(\boldsymbol{\theta})|\hat{\Phi}\right). \tag{9}$$

In the same way that a single output value can be caused by any member of a set of parameter values, a target output distribution $p\left(\boldsymbol{q}|\hat{\Phi}\right)$ can be caused by any member of a set of parameter distributions. To ensure uniqueness of the "posterior" parameter distributions, we must, therefore, specify "prior" distributions for the parameters as in more traditional Bayesian inference. In what follows, we assume the conditional distribution $p\left(\boldsymbol{\theta}|\boldsymbol{q}, \hat{\Phi}\right)$ is independent of the data, i.e. $p\left(\boldsymbol{\theta}|\boldsymbol{q}, \hat{\Phi}\right) = p(\boldsymbol{\theta}|\boldsymbol{q})$, and thus represents a conditional "prior" which can be manipulated using Bayes' rule as,

$$p(\boldsymbol{\theta}|\boldsymbol{q}(\boldsymbol{\theta})) = \frac{p(\boldsymbol{\theta})}{p(\boldsymbol{q}(\boldsymbol{\theta}))}. \tag{10}$$

This results in the form of the posterior parameter distribution targeted by our sampling algorithm,

$$p\left(\boldsymbol{\theta}|\hat{\Phi}\right) = \frac{p(\boldsymbol{\theta})}{p(\boldsymbol{q}(\boldsymbol{\theta}))} p\left(\boldsymbol{q}(\boldsymbol{\theta})|\hat{\Phi}\right). \tag{11}$$

Again, we defer to our companion piece (Lambert et al., 2018) for detailed explanation of Eqs. (10) and (11) and, instead, here provide brief interpretation when considering a uniform prior on parameter space. In this case, $p(\boldsymbol{\theta}) = \frac{1}{V}$, where V is the total volume of parameter space. The denominator term of Eq. (10) is the prior induced on output space by the prior over parameter space. For a uniform prior on parameter values, this is,

$$p(\boldsymbol{\theta}|\boldsymbol{q}(\boldsymbol{\theta})) = \frac{1}{\mathscr{V}(\boldsymbol{q}(\boldsymbol{\theta}))}, \tag{12}$$

where $\mathscr{V}(\boldsymbol{q}(\boldsymbol{\theta}))$ is the volume of parameter space occupied by the iso-output contour $\Omega(\boldsymbol{q}(\boldsymbol{\theta}))$ (see Fig. 3 for the meaning of this volume for a two parameter example). Therefore, a uniform prior over parameter space implies a prior structure where all parameter values producing the same output are given equal weighting.

2.3. Implementation of CMC

Except for some toy examples, the denominator of Eq. (10) cannot be calculated, so exact sampling from the posterior parameter distribution of Eq. (11) is not, in general, possible. We propose, instead, a computationally efficient sampling method to estimate $p(\boldsymbol{q}(\boldsymbol{\theta}))$, which forms the first step of our so-called "Contour Monte Carlo" (CMC) algorithm (Algorithm 1; Fig. 4ii)), where the volume of iso-output contours with each feasible output value is estimated. This step involves repeated independent sampling from the prior distribution of parameters, $\boldsymbol{\theta}^{[i]} \sim p(\boldsymbol{\theta}|\Xi)$, where Ξ parameterises the prior probability density. Each parameter sample is then mapped to an output value, $\boldsymbol{q}^{[i]} = \boldsymbol{q}\left(\boldsymbol{\theta}^{[i]}\right)$. The collection of output samples is then fitted using a vine copula kernel density estimator (KDE) (Nagler and Czado, 2016), $\hat{\Psi} = \underset{\Psi}{\operatorname{argmax}}\ p((\boldsymbol{q}^{[1]}, \ldots, \boldsymbol{q}^{[N_1]})|\Psi)$. Throughout the course of development of CMC, we tested many KDE methods and found vine copula KDE best suited to approximating the higher dimensional probability distributions required in practice – other methods produced coarse estimates of the joint density and took substantially more computational resource. Indeed, the ability to do KDE in high dimensions was the motivation behind the creation of vine copula KDE in the first place (Nagler and Czado, 2016).

The second step in our algorithm then uses MCMC to sample from an approximate version of Eq. (11), where the estimated density, $p\left(\boldsymbol{q}(\boldsymbol{\theta})|\hat{\Psi}\right)$ replaces its corresponding estimand (Algorithm 1; Fig. 4iii)),

$$p\left(\boldsymbol{\theta}|\hat{\Phi}, \Xi, \hat{\Psi}\right) = \frac{p(\boldsymbol{\theta}|\Xi)}{p\left(\boldsymbol{q}(\boldsymbol{\theta})|\hat{\Psi}\right)} p\left(\boldsymbol{q}(\boldsymbol{\theta})|\hat{\Phi}\right). \tag{13}$$

The final step in CMC is to compare output samples generated by MCMC with the target distribution (Fig. 4iv)). As the sample size of both sampling steps (i.e. the contour volume estimation and MCMC steps) tends to infinity, CMC produces a sample of parameter values $(\boldsymbol{\theta}^{[1]}, \boldsymbol{\theta}^{[2]}, \ldots)$ which, when mapped to the output space, corresponds to the target distribution $p\left(\boldsymbol{q}|\hat{\Psi}\right)$. In developing CMC, we found that a finite sample of modest size for both steps of CMC results in parameter samples that, when transformed, often represented good approximations of the target. There are, however, occasions when this is not the case, and this final confirmatory step is indispensable since it frequently highlights inadequacies in contour volume estimation or MCMC, meaning more samples from either or both of these steps are required. It may also be necessary to tweak hyperparameters of the KDE in the contour volume estimation step to ensure reasonable approximation of the distribution of output values obtained by sampling the prior density.

If the target distribution is sensitive to the contour volume estimates, this may also indicate that the target snapshot distribution is incompatible with the model: here, we make no claims on existence of a solution to the inverse problem, only that, Contour Monte Carlo is a pragmatic approach to approximate it by sampling if one should exist. A useful way to diagnose whether the target distribution can be produced from the model and chosen priors is to plot the output values from the contour volume estimation step of CMC: this is akin to visualising the prior predictive distribution in traditional Bayesian inference (Lambert, 2018). If the bulk of target probability mass does not overlap with the simulated output values, then the model and/or chosen prior are unlikely to be invertible to this particular target. In §3.2.2 and §3.4, we provide examples that illustrate this aspect of model checking.

2.4. Workflow and CMC algorithm

A graphical illustration of the complete CMC workflow is provided in Fig. 4. All variables are defined in Table 1. The CMC algorithm is provided in Algorithm 1. In this implementation, MCMC sampling is performed via the Random Walk Metropolis algorithm, but for the examples in §3, we use an adaptive MCMC algorithm to improve sampling efficiency (Johnstone et al., 2016).

To generate our results in §3, we assumed for the contour volume estimation step sample sizes were sufficient if the output samples from MCMC provided a reasonable approximation to the target, although we recognise that future work should refine this process further. For the MCMC step, we used adaptive covariance MCMC (see SOM of Johnstone et al. (2016)) to sample from the target distribution, as it typically provides a considerable speed-up over Random Walk Metropolis (Metropolis et al., 1953; Lambert, 2018). We also used the Gelman-Rubin convergence statistic, $\widehat{R}$, to diagnose convergence (Lambert, 2018; Gelman and Rubin, 1992), with a convergence threshold of $\widehat{R} \leqslant\sim 1.1$.

To solve the forward model of each differential equation, we used Julia's (Bezanson et al., 2017) "solve" method for ODE models from the "DifferentialEquations.jl" library (Rackauckas et al., 2017), which automatically chooses an efficient inbuilt solver. To repli-

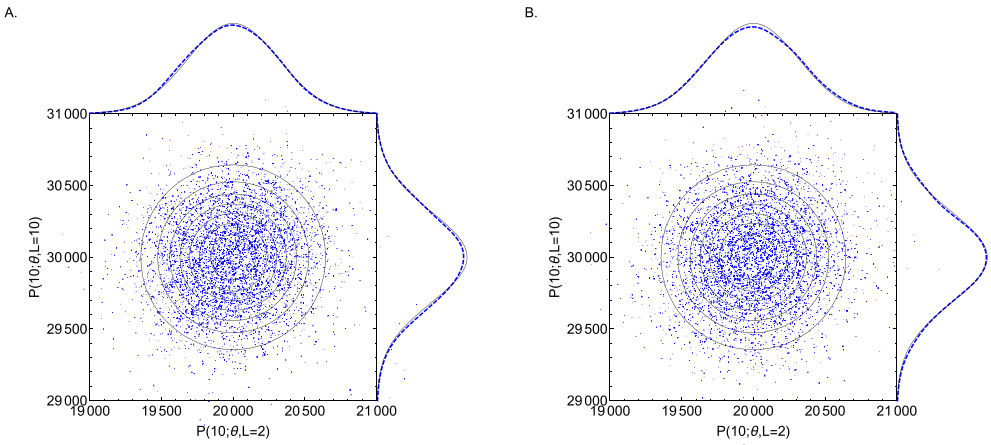

Fig. 5. Growth factor model. Target joint output distribution (solid contour lines) and target marginal distributions (solid lines; above and to the right of each figure) versus outputs sampled by CMC (blue points) and reconstructed marginals (dashed lines). (A) uniform priors. (B) Gaussian priors. In CMC, 100,000 independent samples were used in the "ContourVolumeEstimator" step and 10,000 MCMC samples across each of 4 Markov chains were used in the second step, with the first half of the chains discarded as "warm-up" (Lambert, 2018). For the reconstructed marginal densities in the plots, we use Mathematica's "SmoothKernelDistribution" function specifying bandwidths of 100 with Gaussian kernels (Inc. Wolfram Research, 2020).

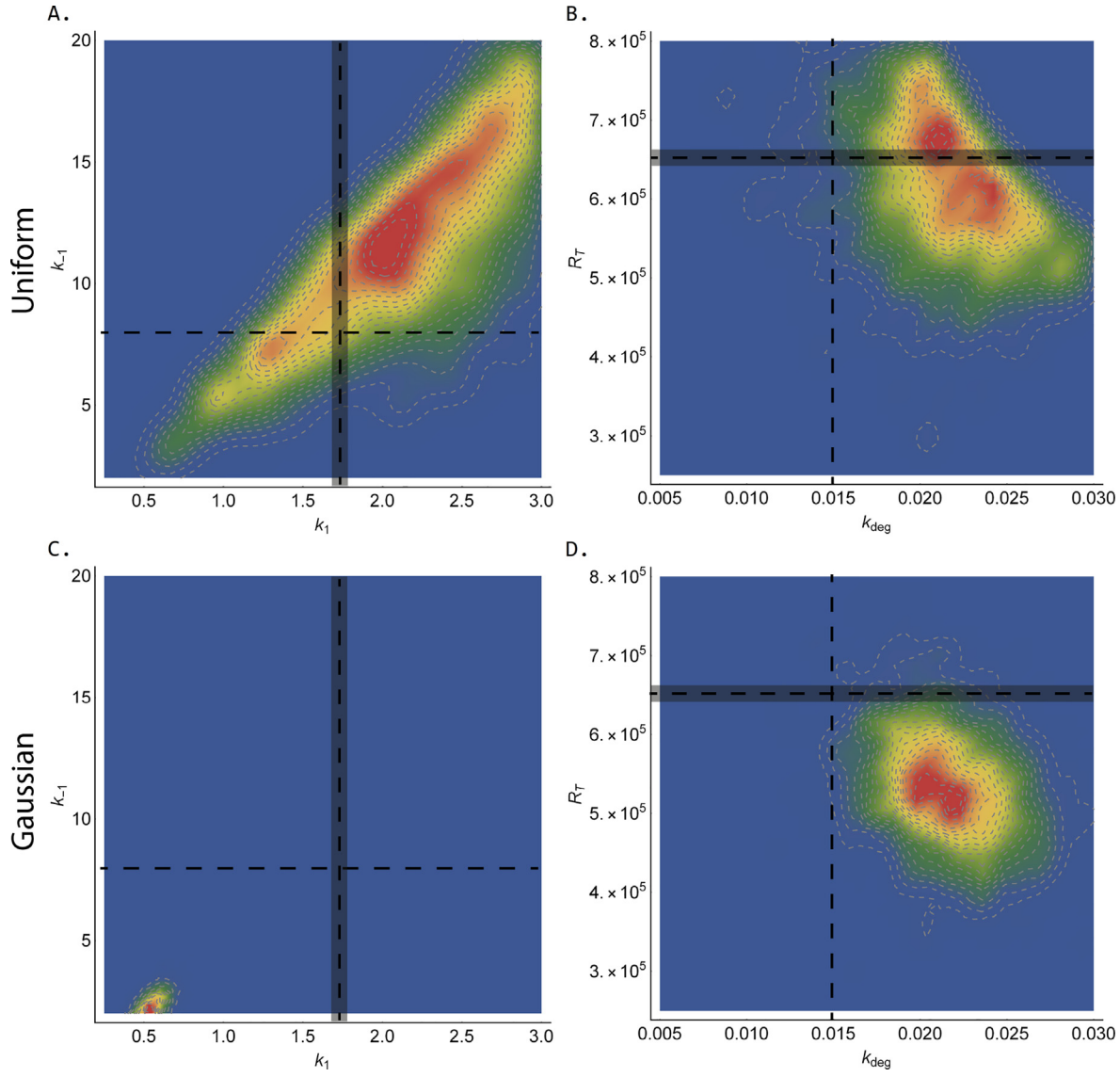

Fig. 6. Growth factor model. Joint posterior distributions estimated by CMC. Top row (A-B): (k_1, k_{-1}) and (k_{deg}, R_T) using uniform priors. Bottom row (C-D): (k_1, k_{-1}) and (k_{deg}, R_T) using Gaussian priors. In all panels, dashed lines indicate the parameter set or distribution used to generate the target distribution given by Eq. (16): for k_{-1} and k_{deg}, the dashed lines show true parameter values and for k_1 and R_T, they show the mean of each Gaussian sampling distributions ($\pm$ two standard deviations shown by shaded rectangles). See Fig. 5 caption for CMC details and Table 3 for the priors used. Red (blue) indicates areas of relatively high (low) probability density.

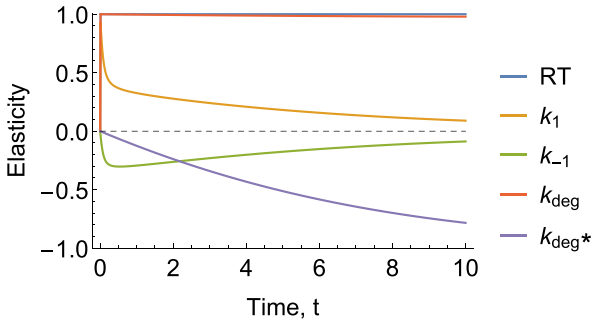

Fig. 7. Growth factor model. Elasticities of the active ligand-bound receptors P with respect to each parameter as a function of time. When calculating the elasticities of each parameter, the other parameters were set to their posterior medians given in Table 2 and $L = 2$.

cate the results in this section, we recommend readers execute the corresponding Julia scripts (one for each result section) at https://github.com/ben18785/inverse-sensitivity/tree/master/examples. Note that, these scripts use the "*RCall*" library for Julia (Bates et al., 2015), which calls R from Julia. This package was necessary to use the "*kdevine*" R package for vine copula kernel density estimation (Nagler, 2018).

3. Results

In this section, we use CMC to estimate posterior parameter distributions for four biological systems. In two of the examples, we assume that the first step of CMC ("SnapshotEstimator" within Algorithm 1) has already been completed, and we are faced with inferring a parameter distribution which, when mapped to outputs, recapitulates the target density. To accompany the text, we provide the Julia notebook used to generate the results. A table of priors used for each example is provided in Table 3.

3.1. Growth factor model

We first consider the "growth factor model" introduced by Dixit et al. (2018), which concerns the dynamics of inactive ligand-free cell surface receptors, R, and active ligand-bound cell surface

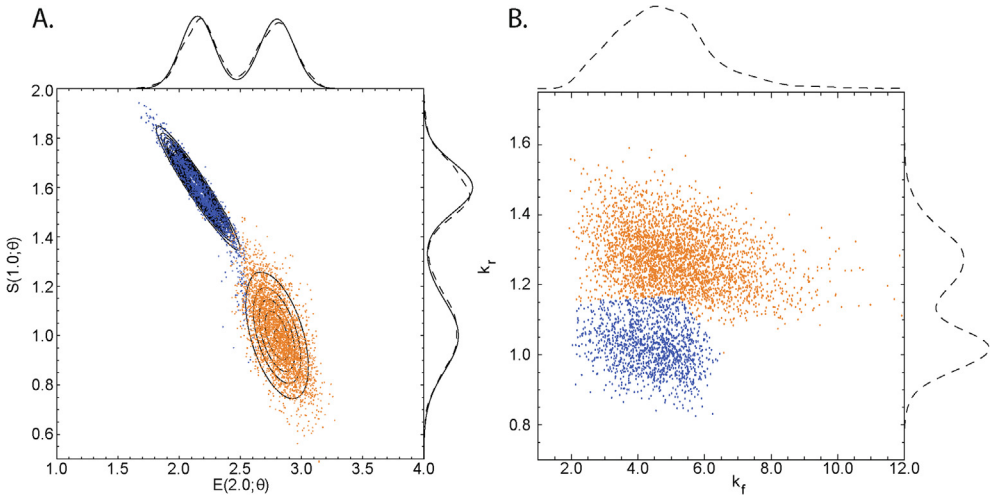

Fig. 8. Michaelis-Menten model. (A) Bimodal target distribution $\boldsymbol{q}$ (solid contour lines) versus output samples (points). (B) posterior parameter samples (points). The solid and dashed lines above and to the side of panel A indicate the target and estimated marginal output distributions, respectively. In B, only estimated parameter marginals are shown as the exact solutions are unknown. The orange (blue) points in A were generated by the orange (blue) parameter samples in B. See Fig. 5 caption for CMC details. Mathematica's "SmoothKernelDistribution" function (Inc. Wolfram Research, 2020) with Gaussian kernels was used to construct marginal densities with: (A) default bandwidths, and (B) bandwidths of 0.3 (horizontal axis) and 0.03 (vertical axis). Mathematica's "ClusteringComponents" function (Inc. Wolfram Research, 2020) was used to identify clusters in B. (For interpretation of the references to colour in this figure legend, the reader is referred to the web version of this article.)

Table 2
Growth factor model. Estimated quantiles from CMC samples with uniform and Gaussian priors. The last column indicates the proportion of the uniform prior bounds occupied by the 25%-75% posterior interval in each case. The prior hyperparameters used in each case are given in Table 3.

Parameter	Quantiles						Posterior 25%–75%
	2.5%	25%	50%	75%	97.5%	True values	conc.
				Uniform prior			
R_T	441,006	548,275	606,439	677,055	772,484	650,000	23%
k_1	0.90	1.69	2.17	2.56	2.95	1.70	32%
k_{-1}	4.35	8.35	11.23	14.23	18.71	8.00	33%
k_{deg}	0.013	0.019	0.021	0.024	0.029	0.015	20%
k^*_{deg}	0.20	0.34	0.40	0.44	0.49	0.25	27%
				Gaussian prior			
R_T	408,396	487,372	529,558	577,970	678,632	650,000	16%
k_1	0.39	0.49	0.54	0.60	0.70	1.70	4%
k_{-1}	1.39	1.92	2.26	2.63	3.35	8.00	4%
k_{deg}	0.016	0.020	0.022	0.024	0.027	0.015	16%
k^*_{deg}	0.22	0.29	0.33	0.38	0.46	0.25	21%

Table 3
Priors used for each example in §3. The parameters θ_1 and θ_2 indicate the prior hyperparameters: for uniform priors, these correspond to the lower and upper limits; for Gaussian priors, they correspond to the mean and standard deviation.

Model	Target density	Parameter	Prior density	Prior θ_1	Prior θ_2
Growth factor	2D Gaussian	R_T	uniform	2.5×10^5	8×10^5
		k_1	uniform	0.25	3.0
		k_{-1}	uniform	2.0	20.0
		k_{deg}	uniform	0.005	0.03
		k^*_{deg}	uniform	0.1	0.5
Growth factor	2D Gaussian	R_T	Gaussian	5×10^5	1×10^5
		k_1	Gaussian	0.5	0.1
		k_{-1}	Gaussian	3.0	1.0
		k_{deg}	Gaussian	0.02	0.005
		k^*_{deg}	Gaussian	0.3	0.1
Michaelis-Menten	bimodal Gaussian	k_f	uniform	0.2	15
		k_r	uniform	0.2	2.0
		k_{cat}	uniform	0.5	3.0
Michaelis-Menten	4D Gaussian	k_f	uniform	0.2	15
		k_r	uniform	0.2	2.0
		k_{cat}	uniform	0.2	3.0
		E_0	uniform	3.0	5.0
		S_0	uniform	5.0	10.0
		C_0	uniform	0.0	0.2
		P_0	uniform	0.0	0.2
TNF signalling	bivariate Gaussian	a_1	uniform	0.4	0.8
		a_2	uniform	0.1	0.7
		a_3	uniform	0.3	0.7
		a_4	uniform	0.1	0.3
		b_1	uniform	0.5	0.7
		b_2	uniform	0.4	0.6
		b_3	uniform	0.4	0.6
		b_4	uniform	0.2	0.4
		b_5	uniform	0.2	0.4
TNF signalling	bimodal Gaussian	a_1	uniform	0.5	0.7
		a_2	uniform	0.1	0.3
		a_3	uniform	0.1	0.3
		a_4	uniform	0.4	0.6
		b_1	uniform	0.3	0.5
		b_2	uniform	0.6	0.8
		b_3	uniform	0.2	0.4
		b_4	uniform	0.4	0.6
		b_5	uniform	0.3	0.5
hESC differentiation	1D-2D Gaussian	p_1	uniform	40.0	60.0
		p_2	uniform	2.0	10.0
		p_3	uniform	0.5	16
		p_4	uniform	0.0	0.7
		p_5	uniform	2.0	4.0
		p_6	uniform	2.0	20.0
		p_7	uniform	0.0	0.2

receptors, P, modulated by an exogenous ligand, L. The governing dynamics are determined by the following system,

$$\frac{dR}{dt} = R_T k_{deg} + k_1 LR(t) + k_{-1} P(t) - k_{deg} R(t) \tag{14}$$

$$\frac{dP}{dt} = k_1 LR(t) - k_{-1} P(t) - k^*_{deg} P(t), \tag{15}$$

with initial conditions,

$$R(0) = 0.0, \qquad P(0) = 0.0,$$

and $\boldsymbol{\theta} = \left(R_T, k_1, k_{-1}, k_{deg}, k^*_{deg}\right)$ are parameters to be determined. In this example, we use measurements of the active ligand-bound receptors P to estimate cellular heterogeneity in these processes. We denote the solution of Eq. (15) as $P(t; \boldsymbol{\theta}, L)$. Here we generate a target model by forward simulations of Eq. (14); in each case recording $(P(10; \boldsymbol{\theta}, 2), P(10; \boldsymbol{\theta}, 10))$. In each forward simulation, we fix $\left(k_{-1}, k_{deg}, k^*_{deg}\right) = (8, 0.015, 0.25)$ and independently sample values $R_T \sim \mathcal{N}\left(6.5 \times 10^5, 0.6 \times 10^4\right)$ and $k_1 \sim \mathcal{N}(1.7, 0.05)$. This generates an output distribution approximately given by,

$$\boldsymbol{q} = \begin{pmatrix} q_1 \\ q_2 \end{pmatrix} = \begin{pmatrix} P(10; \boldsymbol{\theta}, 2) \\ P(10; \boldsymbol{\theta}, 10) \end{pmatrix} \sim \mathcal{N} \left[\begin{pmatrix} 2 \times 10^4 \\ 3 \times 10^4 \end{pmatrix}, \begin{pmatrix} 1 \times 10^5 & 0 \\ 0 & 1 \times 10^5 \end{pmatrix} \right]. \tag{16}$$

We note that, whilst the parameters $\left(k_{-1}, k_{deg}, k^*_{deg}\right)$ are fixed during this step (to generate output distributions), they are allowed to vary in §3.1.1 and §3.1.2 (where we use CMC to perform inference).

3.1.1. Uniform prior

For an under-determined model, the number of QOIs, m, is less than the number of parameters, p, and there typically exists a non-

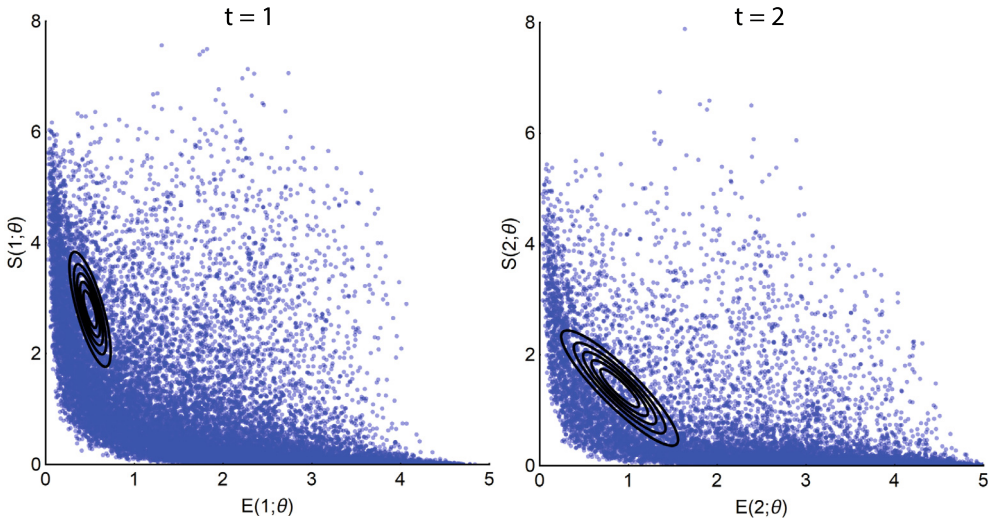

Fig. 9. Michaelis-Menten model. QOIs (blue points) obtained by independently sampling the priors versus the target distribution (black solid contours). Left: (q_1, q_2). Right: (q_3, q_4). We show 20,000 output samples, where each set of four measurements was obtained from a single sample of all parameters. The output target distribution shown by the contours corresponds to the marginal densities of each pair of enzyme-substrate measurements given by Eq. (20). (For interpretation of the references to colour in this figure legend, the reader is referred to the web version of this article.)

singular set of parameter distributions mapping to the same target output distribution. To uniquely identify a posterior parameter distribution, it is, therefore, necessary to specify a prior parameter distribution. By incorporating priors, this allows pre-existing biological knowledge to be included, leading to reduced uncertainty in parameter estimates. CMC allows any prior with correct support to be used. Changes to priors affect both the "ContourVolumeEstimation" and "MCMC" steps of CMC (Algorithm 1), so that the (changed) posterior parameter distribution still maps to the target.

To start, we specify a uniform prior for each of the five parameters, with bounds given in Table 3, and use CMC to estimate the posterior parameter distribution. In Fig. 5A, we show the sampled outputs (blue points) versus the contours of the target distribution (black solid closed curves), illustrating a good correspondence between the sampled and target densities. Above and to the right of the main panel, we also display the marginal target densities (solid black lines) versus kernel density estimator reconstructions of the output marginals from the CMC samples (dashed blue lines), which again highlights the fidelity of the CMC sampled density to the target.

In Fig. 6A, we plot the joint posterior parameter distribution for k_1, the rate of ligand binding to inactive receptors and k_{-1}, which dictates the rate of the reverse reaction. A given level of bound ligands can be generated in many different ways. Not surprisingly, it is the *ratio* of the forward and reverse reaction rates, k_1 and k_{-1} respectively, that is of greatest importance, and because of this, the distribution representing cell process heterogeneity contains linear positive correlations between these parameters.

In Fig. 6B, we show the posterior parameter distribution for k_{deg}, the rate of degradation of ligand-free cell surface receptors and R_T, the rate of introduction of ligand-free cell surface receptors. This plot shows more concentrated posterior mass than in Fig. 6A.

Why do our measurements allow us to better resolve (k_{deg}, R_T) compared to (k_1, k_{-1})? To answer this, it is useful to calculate the sensitivity of $P(t;\boldsymbol{\theta}, L)$ to changes in each of the parameters. To account for the differing magnitudes of each parameter, we calculate elasticities, the proportional changes in measured output for a proportional change in parameter values, using the forward sensitivities method described in Daly et al. (2018), and these are shown in Fig. 7. When the exogenous ligand is set at $L = 2$, these indicate the active ligand-bound receptor concentration is most elastic to changes in R_T and k_{deg}. This higher elasticity means that their range is more restricted by the output measurement than for k_1 and k_{-1}, which have much smaller elasticities at $t = 10$. In Table 2, we show the posterior quantiles for the estimated parameters, and in the last column, indicate the ratio of the 25%-75% posterior interval widths to the uniform prior range for each parameter. These were strongly negatively correlated with the magnitude of the elasticities for each parameter ($\rho = 0.95, t = -5.22, df = 3, p = 0.01$ for Pearson's product-moment correlation), indicating the utility of sensitivity analyses for optimal experimental design, see e.g., Banks et al. (2011). We suggest, however, that CMC can also be used for this purpose. If an experimenter generates synthetic data for various choices of QOIs, they can use CMC to derive the posterior parameter distributions in each case. They then, simply, select the particular QOI producing the narrowest posterior for key parameters.

In both panels of Fig. 6, we also plot the "*actual*" parameter values as dashed lines: for k_{-1} and k_{deg}, these indicate the true (fixed) parameter values, and, for k_1 and R_T, they show the mean of each Gaussian sampling distribution ($\pm$ two standard deviations shown by shaded rectangles). For most parameters, these indicate that the area of highest posterior density is close to the causative parameter values. This is reaffirmed in the top panel of Table 2, where, in all cases, the actual parameter values lie within the estimated 95% quantiles for each parameter – indicating that the parameters were reasonably well identified.

3.1.2. Gaussian prior

We now use CMC to estimate the posterior parameter distribution, when using Gaussian priors (prior hyperparameters shown in Table 3), which are more concentrated than the uniform priors used in §3.1.1. As desired, the target output distribution appears virtually unaffected by the change of priors (Fig. 5B) although with substantial changes to the posterior parameter distribution (Fig. 6C and 6D). In particular, the marginal posterior distributions obtained from the Gaussian prior are narrower compared to the uniform case (rightmost column of Table 2).

As in traditional Bayesian inference, prior choice has a greater influence on the posterior distribution when data provide less information on the underlying process. This is readily apparent in

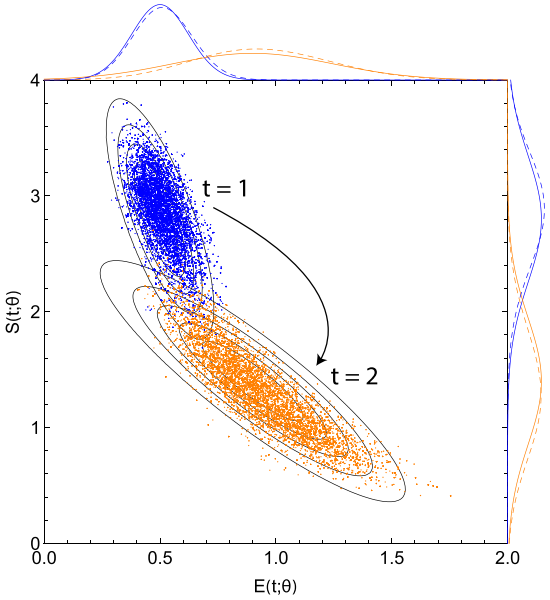

Fig. 10. Michaelis-Menten model. Posterior output samples from CMC (coloured points) versus contour plots (black solid lines) of the joint marginal distributions of Eq. (20). Enzyme and substrate measurements are given by the horizontal and vertical axes, respectively. Output functionals for (q_1, q_2) and (q_3, q_4) are given by blue and orange points, respectively. The solid and dashed coloured lines outside the panels indicate exact target marginals of Eq. (20) and those estimated by CMC, respectively. In the "ContourVolumeEstimator" step, 200,000 independent samples were used, and in the MCMC step, 10,000 samples across each of 4 Markov chains were used, with the first half of the chains discarded as "warm-up" (Lambert, 2018). Mathematica's "SmoothKernelDistribution" function, using Gaussian kernels (Inc. Wolfram Research, 2020) and bandwidths ranging from 0.1 to 0.4, was used to reconstruct marginal densities.

comparing the dramatic change from Fig. 6A to 6C for (k_1, k_{-1}), which have low sensitivities, with the more nuanced change from Fig. 6B to 6D for (k_{deg}, R_T), which have high sensitivities. The results also indicate the bias-variance trade-off inherent in Bayesian analysis: when relatively uninformative priors are specified (Fig. 6A&B), the posterior distributions are wider but their centre lies, in general, closer to the true values (dashed lines) than when more information is included in the priors (Fig. 6C&D).

3.2. Michaelis-Menten kinetics

In this section, we use CMC to invert output measurements from the Michaelis-Menten model of enzyme kinetics (see, for example, Murray, 2007) – illustrating how CMC can determine resolve population substructure from a multimodal output distribution. The Michaelis-Menten model of enzyme kinetics describes the dynamics of concentrations of an enzyme, E, a substrate, S, an enzyme-substrate complex, C, and a product, P,

$$\begin{aligned} \frac{dE}{dt} &= -k_f E(t)S(t) + k_r C(t) + k_{cat} C(t), \\ \frac{dS}{dt} &= -k_f E(t)S(t) + k_r C(t), \\ \frac{dC}{dt} &= k_f E(t)S(t) - k_r C(t) - k_{cat} C(t), \\ \frac{dP}{dt} &= k_{cat} C(t), \end{aligned} \tag{17}$$

with initial conditions,

$$E(0) = E_0,\ S(0) = S_0,\ C(0) = C_0,\ P(0) = P_0, \tag{18}$$

where k_f is the rate of the forward reaction $E + S \to C$, k_r is the rate of the reverse reaction $C \to E + S$, and k_{cat} is the catalytic rate of product formation by the reaction $C \to E + P$.

3.2.1. Bimodal output distribution

When subpopulations of cells, each with distinct dynamics, are thought to exist, determining their characteristics – the proportions of cells in each cluster, their distinct parameter values, and so on – is often of key interest (Hasenauer et al., 2011; Loos et al., 2018). Before formal inference occurs, an output distribution with multiple modes may signal the existence of fragmented subpopulations of cells, and to exemplify this, we target a bimodal bivariate Gaussian distribution for measurements of the level of enzyme and substrate at $t = 1$ and $t = 2$ respectively,

$$\begin{aligned} \boldsymbol{q} = \begin{pmatrix} q_1 \\ q_2 \end{pmatrix} = \begin{pmatrix} E(2.0;\boldsymbol{\theta}) \\ S(1.0;\boldsymbol{\theta}) \end{pmatrix} &\sim p(\boldsymbol{q}; \boldsymbol{\mu}_1, \Sigma_1, \boldsymbol{\mu}_2, \Sigma_2) \\ &= \tfrac{1}{2}\left(\mathcal{N}(\boldsymbol{q}; \boldsymbol{\mu}_1, \Sigma_1) + \mathcal{N}(\boldsymbol{q}; \boldsymbol{\mu}_2, \Sigma_2)\right), \end{aligned} \tag{19}$$

where $\boldsymbol{\theta} = (k_f, k_r, k_{cat})$. The parameters of the Gaussian mixture components are,

$$\boldsymbol{\mu}_1 = \begin{pmatrix} 2.2 \\ 1.6 \end{pmatrix},\ \Sigma_1 = \begin{pmatrix} 0.018 & -0.013 \\ -0.013 & 0.010 \end{pmatrix},$$
$$\boldsymbol{\mu}_2 = \begin{pmatrix} 2.8 \\ 1.0 \end{pmatrix},\ \Sigma_2 = \begin{pmatrix} 0.020 & -0.010 \\ -0.010 & 0.020 \end{pmatrix}.$$

In what follows, we specify uniform priors on each element of $\boldsymbol{\theta}$ (see Table 3). Using a modest number of samples in each step, CMC provides a close approximation to the output target distribution (Fig. 8A). Without providing *a priori* information on the subpopulations of cells, two distinct clusters of cells emerged from applica-

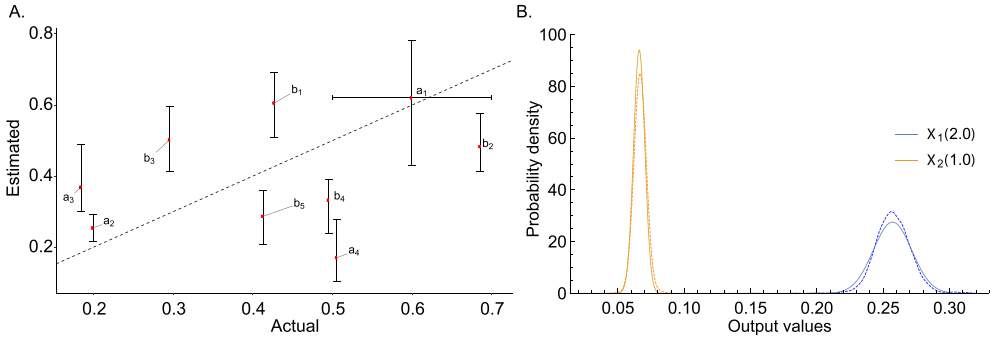

Fig. 11. TNF signalling pathway model. (A) Actual parameter values versus estimated quantiles for the output distribution of Eq. (25). (B) Marginal output targets (solid lines) and sampled output distributions (dashed lines). In A, in the vertical direction, red points indicate 50% posterior quantiles and upper and lower whiskers indicate 97.5% and 2.5% quantiles, respectively; in the horizontal direction, with the exception of a_1, red points indicate the parameter values used to generate the data; for a_1, the red point indicates the mean of the Gaussian distribution used to generate the data and the whiskers indicate its 95% quantiles. In CMC, 10,000 independent samples were used in the "ContourVolumeEstimator" step, and 5,000 MCMC samples across each of 4 Markov chains were used in the second, with the first half of the chains discarded as "warm-up" (Lambert, 2018). Mathematica's "SmoothKernelDistribution" function, using a Gaussian kernel (Inc. Wolfram Research, 2020) and a bandwidth of 0.003 was used to reconstruct marginal densities.

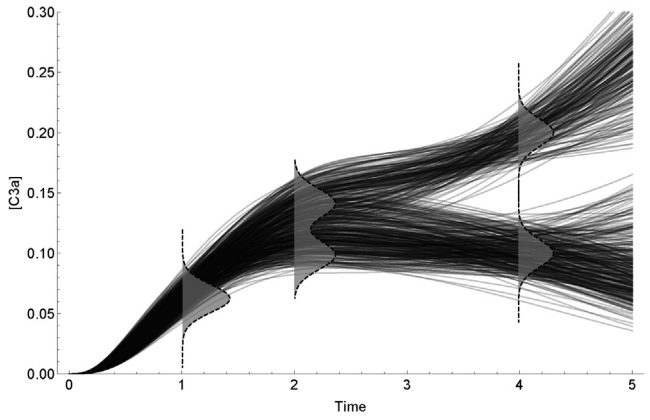

Fig. 12. TNF signalling pathway model. Target output distribution (dashed plots with grey filling) and unique trajectories (black solid lines) obtained from the posterior parameter distribution. In CMC, 10,000 independent samples were used in the "ContourVolumeEstimator" step, and 5,000 MCMC samples across each of 4 Markov chains were used in the second, with the first half of the chains discarded as "warm-up" (Lambert, 2018).

tion of CMC (orange and blue points in Fig. 8A) – each corresponding to distinct modes of the output distribution (corresponding coloured points in Fig. 8A). It is worth noting, however, that the issues inherent with using MCMC to sample multimodal distributions similarly apply here. So, whilst adaptive MCMC (Johnstone et al., 2016) sufficed to explore this posterior surface, it may be necessary to use MCMC methods more robust to such geometries in other cases (for example, population MCMC (Jasra et al., 2007)).

3.2.2. Four-dimensional output distribution

Loos et al. (2018) consider a multidimensional output distribution, with correlations between system characteristics that evolve over time. Our approach allows arbitrary covariance structure between measurements, and to exemplify this, we now target a four-dimensional output distribution, with paired measurements of enzyme and substrate at $t = 1$ and $t = 2$,

$$\boldsymbol{q} = \begin{pmatrix} q_1 \\ q_2 \\ q_3 \\ q_4 \end{pmatrix} = \begin{pmatrix} E(1.0;\boldsymbol{\theta}) \\ S(1.0;\boldsymbol{\theta}) \\ E(2.0;\boldsymbol{\theta}) \\ S(2.0;\boldsymbol{\theta}) \end{pmatrix} \sim \mathcal{N}\left[\begin{pmatrix} 0.5 \\ 2.8 \\ 0.9 \\ 1.4 \end{pmatrix}, \begin{pmatrix} 0.02 & -0.05 & 0.04 & -0.05 \\ -0.05 & 0.30 & -0.15 & 0.20 \\ 0.04 & -0.15 & 0.12 & -0.17 \\ -0.05 & 0.20 & -0.17 & 0.30 \end{pmatrix} \right]. \tag{20}$$

Since this target has four QOIs, and the Michaelis-Menten model has three rate parameters (k_f, k_r, k_{cat}), the system is over-identified, and so CMC cannot be straightforwardly applied. The initial concentrations of species in cellular assays are measured quantities – that is, imperfect representations of the underlying quantities. We prefer to estimate them through inference rather than fix them as this better reflects reality. So, we allow the four initial states (E_0, S_0, C_0, P_0) to be uncertain quantities, bringing the total number of parameters to seven.

We set uniform priors on all parameters (see Table 3). In order to check that the model and priors were consistent with the output distribution given by Eq. (20), we plotted the output measurements used to estimate contour volumes (obtained from the first step of the "ContourVolumeEstimator" method in Algorithm 1) against the target (Fig. 9). Since the main support of the densities (black contours) lies within a region of output space reached by independent sampling of the priors (blue points), this indicated the target could feasibly be generated from this model and priors, and we proceeded to estimation by CMC.

Fig. 10 plots the output samples of enzyme and substrate from the last step of CMC for $t = 1$ (blue points) and $t = 2$ (orange points) versus the contours (black lines) of the joint marginal distributions of Eq. (20). The distribution of paired enzyme-substrate samples illustrates that the CMC output distribution closely approximates the target density, itself representing dynamic evolution of the covariance between enzyme and substrate measurements. Target marginal distributions (solid lines) along with their

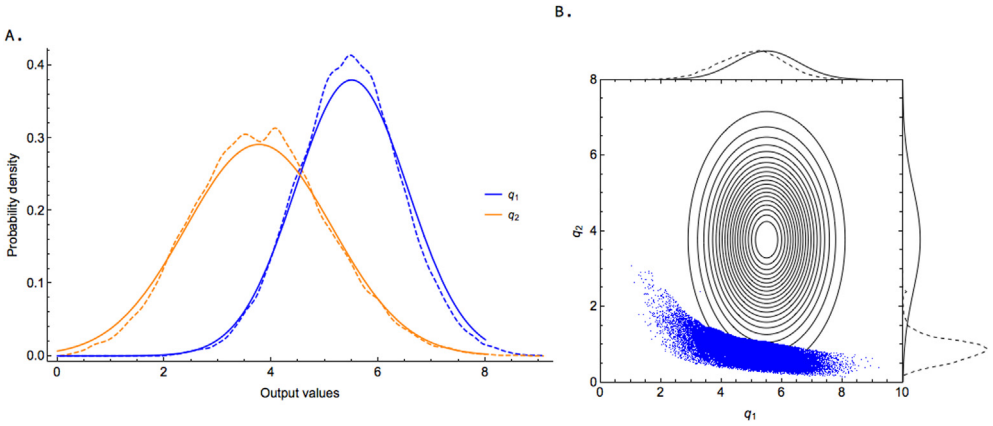

Fig. 13. Embryonic stem cell differentiation model: output targets. In A., we show the output target distributions described in §3.4 and kernel density estimates of the distributions reconstructed from the CMC samples. In B., we show the joint target distribution (contour lines) for the case where we target both q_1 and q_2 simultaneously; above and to the right of the plot, we show the target marginals (solid lines) and the marginals reconstructed from the samples (dashed lines). In CMC, 50,000 independent samples were used in the "ContourVolumeEstimator" step, and 50,000 MCMC samples across each of 4 Markov chains were used in the second, with the first half of the chains discarded as "warm-up" (Lambert, 2018). Mathematica's "SmoothKernelDistribution" function, using a Gaussian kernel (Inc, 2020) and default bandwidths were used to reconstruct marginal densities.

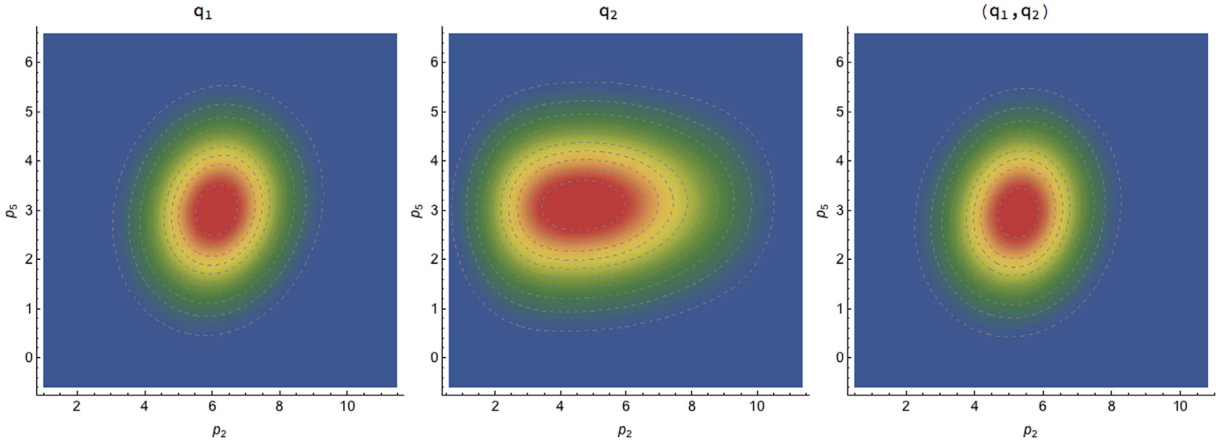

Fig. 14. Embryonic stem cell differentiation model: posterior parameter distribution. In the left panel, we show the posterior distribution for (p_2, p_5) when targeting q_1; in the middle, we show the same when targeting q_2; and in the right panel, we show the same when targeting (q_1, q_2). In CMC, 50,000 independent samples were used in the "ContourVolumeEstimator" step, and 50,000 MCMC samples across each of 4 Markov chains were used in the second, with the first half of the chains discarded as "warm-up" (Lambert, 2018).

approximations from kernel density estimation (dashed lines) are also shown above and to the right of the main panel of Fig. 10 and largely indicate correspondence.

3.3. TNF signalling pathway

We now illustrate how CMC can be applied to another ODE system: the tumour necrosis factor (TNF) signalling pathway model introduced in Chaves et al. (2008) and used by Hasenauer et al. (2011) to illustrate a Bayesian approach to cell population variability estimation. The model incorporates known activating and inhibitory interactions between four key species within the TNF pathway: active caspase 8, x_1, active caspase 3, x_2, a nuclear transcription factor, x_3 and its inhibitor, x_4, such that

$$\begin{aligned} \frac{dx_1}{dt} &= -x_1(t) + \tfrac{1}{2}[\beta_4(x_3(t))\alpha_1(u(t)) + \alpha_3(x_2(t))] \\ \frac{dx_2}{dt} &= -x_2(t) + \alpha_2(x_1(t))\beta_3(x_3(t)) \\ \frac{dx_3}{dt} &= -x_3(t) + \beta_2(x_2(t))\beta_5(x_4(t)) \\ \frac{dx_4}{dt} &= -x_4(t) + \tfrac{1}{2}[\beta_1(u(t)) + \alpha_4(x_3(t))], \end{aligned} \tag{21}$$

with initial conditions,

$$x_1(0) = 0.0, \quad x_2(0) = 0.0, \quad x_3(0) = 0.29, \quad x_4(0) = 0.625. \tag{22}$$

The functions α_i and β_j represent activating and inhibitory interactions respectively,

$$\begin{aligned} \alpha_i(z) &= \frac{z^2}{a_i^2 + z^2}, \quad i = 1, \ldots, 4, \\ \beta_j(z) &= \frac{b_j^2}{b_j^2 + z^2}, \quad j = 1, \ldots, 5, \end{aligned} \tag{23}$$

and the parameters a_i for $i \in (1,2,3,4)$ and b_j for $j \in (1,2,3,4,5)$ represent activation and inhibition thresholds. The function $u(t)$ represents a TNF stimulus represented by a top hat function,

$$u(t) = \begin{cases} 1, & \text{if} \quad t \in [0,2]. \\ 0, & \text{otherwise}. \end{cases} \tag{24}$$

3.3.1. Recovering parameter values in under-determined systems

In under-determined models, a set of parameters of non-zero volume can produce the same output values. A consequence of this unidentifiability is that we cannot perform "full circle" inference: that is, using a known parameter distribution to generate an output distribution does not result in that parameter distribution being recovered through inference. We illustrate this idea by generating an output distribution by varying a single parameter value between runs of the forward model (21) and performing inference on all nine system parameters, whilst collecting only two output measurements. Specifically, we randomly sample $a_1 \sim \mathcal{N}(0.6, 0.05)$ for each simulation of the forward model, whilst holding the other parameters constant,

$$(a_2, a_3, a_4, b_1, b_2, b_3, b_4, b_5) = (0.2, 0.2, 0.5, 0.4, 0.7, 0.3, 0.5, 0.4),$$

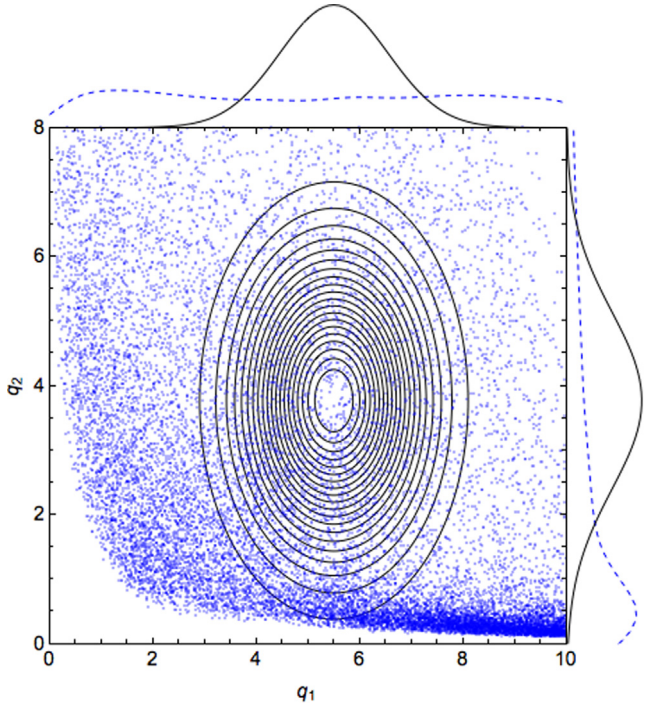

Fig. 15. Embryonic stem cell differentiation model: contour volume distribution. In the main panel, we plot contours (solid black lines) for the joint target distribution of (q_1, q_2) and 20,000 samples from the contour volume estimation step of Algorithm 1 (blue points). Above and to the right of the main panel, we plot the marginal target distribution in each dimension (solid black lines) and the marginal contour volume distributions (dashed blue lines). (For interpretation of the references to colour in this figure legend, the reader is referred to the web version of this article.)

and measure $q_1 = x_1(2.0)$ and $q_2 = x_2(1.0)$ in each case. In doing so, we obtain an output distribution well-approximated by the bivariate Gaussian distribution,

$$\begin{aligned}\boldsymbol{q} &= \begin{pmatrix} q_1 \\ q_2 \end{pmatrix} = \begin{pmatrix} x_1(2.0) \\ x_2(1.0) \end{pmatrix} \\ &\sim \mathcal{N}\left[\begin{pmatrix} 0.26 \\ 0.07 \end{pmatrix}, \begin{pmatrix} 2.1\times10^{-4} & 5.9\times10^{-5} \\ 5.9\times10^{-5} & 1.8\times10^{-5} \end{pmatrix} \right].\end{aligned} \tag{25}$$

We now apply CMC to the target output distribution given by Eq. (25) to estimate a posterior distribution over all nine parameters of Eq. (21). Apart from a few cases, the priors for each parameter were chosen to *exclude* the values that were used to generate the output distribution (see Table 3) to illustrate how the recovered posterior distribution and data generating distribution differ. In Fig. 11A, we plot the actual parameter values (horizontal axis) used to generate the data versus the estimated values (vertical axis). This illustrates that, due to the chosen priors, there is a disjunction between actual and estimated parameter values in all cases apart from a_1. Though, because the model is underdetermined, the corresponding output distribution closely approximates the target despite these differences (Fig. 11B).

3.3.2. Bimodal output distribution

The dynamics of all cells can often be modelled by assuming cells exist in subpopulation clusters, which evolve differently over time. A hint that such subpopulation structure may exist is output distributions with multiple modes. We now apply CMC to investigate a bimodal output distribution for the TNF signalling pathway model similar to that investigated by Hasenauer et al. (2011). We aim to estimate the posterior parameter distribution mapping to the following output distribution,

$$\boldsymbol{q} = \begin{pmatrix} q_1 \\ q_2 \\ q_3 \end{pmatrix}, \tag{26}$$

where,

$$\begin{aligned} q_1 &= \boldsymbol{x}_2(1.0) && \sim \mathcal{N}(0.06, 0.01) \\ q_2 &= \boldsymbol{x}_2(2.0) && \sim \tfrac{1}{2}(\mathcal{N}(0.1, 0.01) + \mathcal{N}(0.14, 0.01)) \\ q_3 &= \boldsymbol{x}_2(4.0) && \sim \tfrac{1}{2}(\mathcal{N}(0.1, 0.01) + \mathcal{N}(0.20, 0.01)), \end{aligned} \tag{27}$$

where the target distributions for $\boldsymbol{q}_2(2.0)$ and $\boldsymbol{q}_2(4.0)$ indicate mixtures of univariate Gaussians, and the priors used are given in Table 3. This target distribution, along with the unique trajectories obtained by applying the CMC algorithm, are shown in Fig. 12. This figure illustrates that a bimodal output distribution causes CMC to sample clusters of parameter values without the need for subpopulation information to be provided ahead of estimation.

3.4. Embryonic stem cell differentiation

We now demonstrate how CMC can be applied to real data generated from experiments investigating human embryonic stem cell (hESC) differentiation. Specifically, we use a reaction kinetics-based model presented in Tu et al. (2019), which seeks to explain regulation of three transcription factors involved in hESC fate: CDH1, ZEB1 and KLF8. The regulation of these three transcription factors was modelled by the following ODE system involving a number of Michaelis-Menten-type terms,

$$\begin{aligned} \tfrac{dC}{dt} &= \tfrac{k_1}{k_2+Z^2} + \tfrac{k_3}{k_4+K^2} - d_1 C \\ \tfrac{dZ}{dt} &= \tfrac{ak_5K^2}{k_6+K^2} - d_2 Z \\ \tfrac{dK}{dt} &= \tfrac{rk_7}{k_8+C^2} - d_3 K, \end{aligned} \tag{28}$$

where $C = [\text{CDH1}], Z = [\text{ZEB1}]$ and $K = [\text{KLF8}]$, subject to initial conditions: $C(0) = C_0, Z(0) = Z_0, K(0) = K_0$, and $a = 1$ and $r = 1$ are nondimensional parameters. We recast this system, using nondimensional variables

$$y_1 = \frac{k_2 d_1}{k_1} C,\ y_2 = \frac{k_6 d_1}{k_4 k_5} Z,\ y_3 = \frac{1}{\sqrt{k_4}} K, \tag{29}$$

and time scale $\frac{1}{d_1}$, so that $\tau = d_1 t$, which results in the following system,

$$\begin{aligned} \tfrac{dy_1}{d\tau} &= \tfrac{1}{1+p_1 y_2^2} + \tfrac{p_2}{1+y_3^2} - y_1 \\ \tfrac{dy_2}{d\tau} &= \tfrac{y_3^2}{1+p_3 y_3^2} - p_4 y_2 \\ \tfrac{dy_3}{d\tau} &= \tfrac{p_5}{p_6+y_1^2} - p_7 y_3, \end{aligned} \tag{30}$$

with initial states $y_1(0) = y_{1,0}, y_2(0) = y_{2,0}, y_3(0) = y_{3,0}$. (See supplementary files for further details.)

In what follows, we perform parameter inference for Eq. (30) on single-cell RNA-seq data obtained and processed as described in Tu et al. (2019) from NCBI's Gene Expression Omnibus. The dataset has single-cell gene expression data for 758 cells collected at six times during the course of experiment (0 h, 12 h, 24 h, 36 h, 72 h, 96 h) for [CDH1], [ZEB1] and [KLF8] with 92, 102, 66, 172, 138 and 188 measurements at each time point respectively.

Here, we consider estimating the posterior parameter distributions using data obtained at $t = 12$h for CDH1 and $t = 72$h for KLF8. Across the three cases described below, we use CMC with priors for parameters in Eq. (30) as given in Table 3. We assume the initial values of each variable are given by: $y_1(0) = 1.5, y_2(0) = 0.0$, $y_3(0) = 0.0$.

We first consider the CDH1 data in isolation. To do so, we fit a Gaussian distribution to these data and obtain $q_1 = y_1(12) \sim \mathcal{N}(5.50, 1.05)$. CMC produces samples that closely approximate this distribution (Fig. 13A; blue lines). The joint posterior distribution for two model parameters, (p_2, p_5), is shown in the leftmost panel of Fig. 14 and shows a concentrated distribution.

Next we consider the KLF8 data alone. We fit a Gaussian distribution to these data and obtain $q_2 = y_3(72) \sim \mathcal{N}(3.77, 1.37)$. Again, using CMC, we obtain samples that closely approximates this target (Fig. 13A; orange lines). The posterior distribution for (p_2, p_5) is, however, now quite different to previously (Fig. 14 middle panel) hinting that it may be quite difficult to determine a posterior distribution where we target both q_1 and q_2.

Finally, we attempt to target the distribution described by both q_1 and q_2. Here, we assume that there is no correlation between these targets because we have no cells with observations for both $t = 12$ and $t = 72$ since the measurement process is destructive. In Fig. 13B, we plot the joint target distribution and samples from CMC. In this plot, it is clear that there is a disjunction between the target distribution and the samples. In particular, the target distribution for q_2 has a mean that is far below the target value.

The rightmost panel of Fig. 14 shows the posterior parameter distribution for (p_2, p_5) when targeting this bivariate output distribution. In comparing it to the other panels in the same figure, it is clear that the posterior distribution when targeting (q_1, q_2) is somewhere between the distributions obtained when targeting q_1 and q_2 in isolation; unfortunately, this midway house is not suited to either case. Indeed, this failure to target both q_1 and q_2 simultaneously suggests that the model does not actually cohere with the data.

To investigate this further, we overlay samples (blue points) from the contour volume estimation step of Algorithm 1 on the joint target distribution of (q_1, q_2) in Fig. 15. In the main panel, the output samples are concentrated in a band that runs from the top left of the plot towards the lower right. Because of this, there is relatively low overlap between the joint target and the contour volumes, indicating that the model does not cohere well with the data and illustrates why inference struggles to find a posterior distribution consistent with the joint target. However, as illustrated in Fig. 13A, it is possible to find posterior distributions consistent with the target distributions for either q_1 or q_2 in isolation. Fig. 15 indicates why this is the case. Above the main panel, we plot these target distributions (black solid lines) and the corresponding contour volume distributions (blue dashed lines). There is considerably more overlap in these marginals than in the joint densities, which shows that finding a posterior consistent with each of these targets in isolation is possible but with them both is tricky. Overall, it appears that the model is not consistent with the data.

By "model" here, it could either be that the ODE system described in Eq. (30) is inappropriate; it is also possible that this could be due to failure to include noise in the measurement process. Given the extent of the discrepancy between the ODE means and the target contours, we suggest that it's most likely that the ODE model misses or misrepresents key processes. These results illustrate how CMC can be used to determine when a model is inconsistent with data and also suggest that extending CMC to handle noisy measurement is likely worthwhile.

4. Discussion

Determining the cause of variability in cellular processes is crucial in many applications, ranging from bioengineering to drug development. In this paper, we introduce a Bayesian method for estimating cellular heterogeneity from "snapshot" measurements of cellular properties taken at discrete intervals during experiments. Our approach assumes what we call a "heterogeneous ordinary differential equation" (HODE) framework, in which biochemical processes in all cells are governed by a common ODE. In HODEs, each cell has different rate parameter values causing a variety of measurements to be obtained across cells. In this framework, estimating heterogeneity in cellular processes amounts to determining the probability distributions of parameter values of the governing ODE. Our method of estimation is a two-step Monte Carlo sampling process we term "Contour Monte Carlo" (CMC), which does not require the number of cell clusters to be provided before estimation, unlike in other approaches. CMC can be used to process high volumes of individual cellular measurements since the framework involves fitting a kernel density estimator to raw experimental data and using these distributions rather than data as the target outcome. CMC can handle arbitrary multivariate structure in measured outputs, meaning it can capture correlations between the same cellular species at different timepoints or, for example, contemporaneous correlations between different cellular compartments. Being a Bayesian approach, CMC uses prior distributions over parameter values to ensure uniqueness of the posterior distribution allowing pre-experimental knowledge to be used to improve estimation robustness. The flexible and robust framework that CMC provides means it can be used to perform automatic inference for wide-ranging systems of practical interest.

Our approach also provides a natural way to test that the process is working satisfactorily. Feeding posterior parameter samples obtained by CMC into forward model simulations results in a distribution of output values which can be compared to the target. Indeed, we have found this comparison indispensable in applying CMC in practice and include it as the last step in the CMC algorithm (Algorithm 1). Discrepancies between the target output distribution and its CMC approximation can occur either as a result of poor estimates of the "contour volume distribution" in the first stage of the algorithm or due to insufficient MCMC samples in the second. Either of these issues are often easily addressed by increasing sample sizes or changing hyperparameter settings for the kernel density estimator. Although kernel density estimation in high dimensional spaces remains an open research problem, we have found vine copula kernel density estimation works well for the dimensionality of output measurements we investigate here (Nagler and Czado, 2016).

Failure to reproduce a given output distribution can also indicate that the generating model (the priors and the forward model) are incongruent with experimental results. This may either be due to misspecification of the ODE system or because the assumption of a deterministic forward model is inappropriate. Our approach currently assumes that output variation is dominated by cellular variation in the parameter values of the underlying ODE with measurement noise making a negligible contribution. Whether this is a reasonable assumption depends on the system under investigation and, more importantly, on experimental details. We recognise that neglecting measurement noise when it is, in fact, important in determining observed data means CMC will overstate cellular variation. It may also mean that some output distributions cannot be obtained by our model system (i.e. HODEs without noise). Future work incorporating a stochastic noise process or, more generally, including stochastic cellular mechanisms is thus likely to be worthwhile.

In Fig. 4, we present the workflow for our approach, which includes as its last step comparing output samples with the target distribution. As discussed above, if output samples do not correspond with the target, this may indicate that a model isn't fit for purpose. Conversely, if there is correspondence with the target distribution, it is possible that a simplified model – with (say) one or more fewer parameters – could also recapitulate the same results. Thus, a process of repeated rounds of model simplification then CMC could be pursued to simplify a model until output samples no longer correspond with the target. The most parsimonious model would then be the simplest case where the output samples still match the target. We note however, that such an approach may be dangerous if the most parsimonious model is then used to predict the distributions of other functionals.

Whilst we have illustrated our approach by fitting ODE models to data, we recognise that our approach is applicable to deterministic forward models in general. These include a large swathe of models used in computational biology, such as partial differential equations and difference equations. Similarly, whilst we have illustrated our approach by fitting to models with time-invariant parameters, it could also be used to determine how parameters vary throughout the course of an experiment – provided the dynamic evolution of parameter values is itself parameterised.

We have labelled our approach as Bayesian since it involves explicit estimation of probability distributions and requires priors. We recognise, however, that it is not of the form used in traditional Bayesian inference. This is because, rather than aiming to formulate a model that describes output observations, our approach aims to recapitulate output *distributions*. Others Butler et al. (2018), (including us Lambert et al., 2018), have considered similar problems before; perhaps most notably by Albert Tarantola in his landmark work on inverse problem theory (see, for example, Tarantola, 2005). In Tarantola's framework, a joint input parameter and output space is considered, where prior knowledge and experimental theory combine elegantly to produce a posterior distribution whose marginal output distribution is a weighted "conjunction"

of various sources of information. This work has seen considerable interest in areas such as the geosciences (Mosegaard and Tarantola, 1995; Vukicevic and Posselt, 2008), and we propose that Tarantola's approach may prove useful for the biosciences.

The natural world is rife with variation, and mathematical models represent frameworks for understanding its causes. Typically, the state of biological knowledge is such that one effect – a given pattern of variation – has many possible causes. Observational or experimental data can be used to apportion weight to each cause in a process that amounts to solving an inverse problem. The approach we describe here follows the Bayesian paradigm of inverse problem solving where uncertainty in potential causes (i.e. parameter values) is described using probability distributions. Here, we illustrate the worth of our method by using it to estimate cellular heterogeneity in biochemical processes. However, it could equally be used to invert other classes of under-determined systems arising elsewhere. Contour Monte Carlo provides an automatic framework for performing inference on such under-determined systems, and the use of priors allows for robust and precise parameter estimation unattainable through the data alone.

Author contributions

BL, DJG and SJT conceived the study. BL carried out the analysis. All authors helped to write and edit the manuscript.

Declaration of Competing Interest

The authors declare that they have no known competing financial interests or personal relationships that could have appeared to influence the work reported in this paper.

Appendix A. Supplementary data

Supplementary data associated with this article can be found, in the online version, at https://doi.org/10.1016/j.jtbi.2020.110541.

References

Altrock, P.M., Liu, L.L., Michor, F., 2015. The mathematics of cancer: integrating quantitative models. Nat. Rev. Cancer 15 (12), 730.

Altschuler, S.J., Wu, L.F., 2010. Cellular heterogeneity: do differences make a difference? Cell 141 (4), 559–563.

Banks, H.T., Holm, K., Kappel, F., 2011. Comparison of optimal design methods in inverse problems. Inverse Prob. 27, 1–31.

Bates, D., Lai, R., Byrne, S., et al., 2015. Rcall. URL: https://github.com/JuliaInterop/RCall.jl. .

Bezanson, J., Edelman, A., Karpinski, S., Shah, V.B., 2017. Julia: a fresh approach to numerical computing. SIAM Rev. 59 (1), 65–98.

Butler, T., Jakeman, J., Wildey, T., 2018. Combining push forward measures and Bayes rule to construct consistent solutions to stochastic inverse problems. SIAM J. Sci. Comput. 40 (2), A984–A1011.

Chan, Y.H., Intosalmi, J., Rautio, S., Lähdesmäki, H., 2016. A subpopulation model to analyze heterogeneous cell differentiation dynamics. Bioinformatics 32 (21), 3306–3313.

Chang, H.H., Hemberg, M., Barahona, M., Ingber, D.E., Huang, S., 2008. Transcriptome-wide noise controls lineage choice in mammalian progenitor cells. Nature 453 (7194), 544.

Chaves, M., Eissing, T., Allgower, F., 2008. Bistable biological systems: a characterization through local compact input-to-state stability. IEEE Trans. Autom. Control 53, 87–100.

Daly, A.C., Gavaghan, D.J., Cooper, J., Tavener, S.J., 2018. Inference-based assessment of parameter identifiability in nonlinear biological models. J. R. Soc. Interface 15. .

Delvigne, F., Zune, Q., Lara, A.R., Al-Soud, W., Sørensen, S.J., 2014. Metabolic variability in bioprocessing: implications of microbial phenotypic heterogeneity. Trends Biotechnol. 32 (12), 608–616.

Dharmarajan, L., Kaltenbach, H.M., Rudolf, F., Stelling, J., 2019. A simple and flexible computational framework for inferring sources of heterogeneity from single-cell dynamics. Cell Syst. 8 (1), 15–26.

Dixit, P., Lyashenko, E., Niepel, M., Vitkup, D., 2018. Maximum entropy framework for inference of cell population heterogeneity in signaling network dynamics. bioRxiv 137513..

Elowitz, M.B., Levine, A.J., Siggia, E.D., Swain, P.S., 2002. Stochastic gene expression in a single cell. Science 297 (5584), 1183–1186.

Erban, R., Chapman, J., Maini, P., 2007. A practical guide to stochastic simulations of reaction-diffusion processes. arXiv preprint arXiv:0704.1908. .

Fraser, D., Kaern, M., 2009. A chance at survival: gene expression noise and phenotypic diversification strategies. Mol. Microbiol. 71 (6), 1333–1340.

Fritzsch, F.S.O., Dusny, C., Frick, O., Schmid, A., 2012. Single-cell analysis in biotechnology, systems biology, and biocatalysis. Annu. Rev. Chem. Biomol. Eng. 3, 129–155.

Gatenby, R.A., Smallbone, K., Maini, P.K., Rose, F., Averill, J., Nagle, Raymond B, Worrall, L., Gillies, R.J., 2007. Cellular adaptations to hypoxia and acidosis during somatic evolution of breast cancer. Br. J. Cancer 97 (5), 646.

Gelman, A., Rubin, D.B., 1992. Inference from iterative simulation using multiple sequences. Stat. Sci., 457–472

Hasenauer, J., Waldherr, S., Doszczak, M., Radde, N., Scheurich, P., Allgöwer, F., 2011. Identification of models of heterogeneous cell populations from population snapshot data. BMC Bioinformatics 12 (1), 125.

Hasenauer, J., Hasenauer, C., Hucho, T., Theis, F.J., 2014. ODE constrained mixture modelling: a method for unraveling subpopulation structures and dynamics. PLOS Comput. Biol. 10, (7) e1003686.

Hilsenbeck, O., Schwarzfischer, M., Skylaki, S., Schauberger, B., Hoppe, P.S., Loeffler, D., Kokkaliaris, K.D., Hastreiter, S., Skylaki, E., Filipczyk, A., et al., 2016. Software tools for single-cell tracking and quantification of cellular and molecular properties. Nat. Biotechnol. 34 (7), 703.

Hughes, A.J., Spelke, D.P., Xu, Z., Kang, C.C., Schaffer, D.V., Herr, A.E., 2014. Single-cell western blotting. Nat. Methods 11 (7), 749.

Inc. Wolfram Research. Mathematica 8.0. https://www.wolfram.com. .

Jasra, A., Stephens, D.A., Holmes, C.C., 2007. On population-based simulation for static inference. Stat. Comput. 17 (3), 263–279.

Johnstone, R.H., Chang, E.T.Y., Bardenet, R., De Boer, T.P., Gavaghan, D.J., Pathmanathan, P., Clayton, R.H., Mirams, G.R., 2016. Uncertainty and variability in models of the cardiac action potential: can we build trustworthy models? J. Mol. Cell. Cardiol. 96, 49–62.

Karlsson, M., Janzén, D.L., Durrieu, L., Colman-Lerner, A., Kjellsson, M.C., Cedersund, G., 2015. Nonlinear mixed-effects modelling for single cell estimation: when, why, and how to use it. BMC Syst. Biol. 9 (1), 52.

Lambert, B., 2018. A Student's Guide to Bayesian Statistics. Sage Publications Ltd..

Lambert, B., Gavaghan, D., Tavener, S.J., 2018. Inverse sensitivity analysis of mathematical models avoiding the curse of dimensionality. BioRxiv 432393. .

Loos, C., Moeller, K., Fröhlich, F., Hucho, T., Hasenauer, J., 2018. A hierarchical, data-driven approach to modeling single-cell populations predicts latent causes of cell-to-cell variability. Cell Syst. 6 (5), 593–603.

Metropolis, N., Rosenbluth, A.W., Rosenbluth, M.N., Teller, A.H., Teller, E., 1953. Equation of state calculations by fast computing machines. J. Chem. Phys. 21 (6), 1087–1092.

Mosegaard, K., Tarantola, A., 1995. Monte Carlo sampling of solutions to inverse problems. J. Geophys. Res.: Solid Earth 100 (B7), 12431–12447.

Murray, J.D., 2007. Mathematical biology: I. An Introduction (interdisciplinary applied mathematics) (Pt. 1). Springer, New York.

Nagler, T., 2018. kdevine: Multivariate Kernel Density Estimation with Vine Copulas, 2018. R package version 0.4.2. .

Nagler, T., Czado, C., 2016. Evading the curse of dimensionality in nonparametric density estimation with simplified vine copulas. J. Multivariate Anal. 151, 69–89.

Rackauckas, C., Nie, Q., 2017. Differentialequations. jl–a performant and feature-rich ecosystem for solving differential equations in julia. J. Open Res. Software 5(1). .

Ramkrishna, D., Singh, M.R., 2014. Population balance modeling: current status and future prospects. Annu. Rev. Chem. Biomol. Eng. 5, 123–146.

Ridley, M., 1994. The red queen: sex and the evolution of human nature. Penguin UK. .

Tarantola, A., 2005. Inverse Problem Theory and Methods for Model Parameter Estimation, vol. 89. SIAM.

Telford, W.G., Hawley, T., Subach, F., Verkhusha, V., Hawley, R.G., 2012. Flow cytometry of fluorescent proteins. Methods 57 (3), 318–330.

Tu, X., Zhang, Q., Zhang, W., Zou, X., 2019. Single-cell data-driven mathematical model reveals possible molecular mechanisms of embryonic stem-cell differentiation. Math. Biosci. Eng. 16 (5), 5877–5896.

Vukicevic, T., Posselt, D., 2008. Analysis of the impact of model nonlinearities in inverse problem solving. J. Atmos. Sci. 65 (9), 2803–2823.

Waldherr, S., 2018. Estimation methods for heterogeneous cell population models in systems biology. J. R. Soc. Interface 15 (147), 20180530.

Zechner, C., Unger, M., Pelet, S., Peter, M., Koeppl, H., 2014. Scalable inference of heterogeneous reaction kinetics from pooled single-cell recordings. Nat. Methods 11 (2), 197.